

NASA Contractor Report 4253

Rapidly Solidified Titanium Alloys by Melt Overflow

Thomas A. Gaspar, Thomas J. Bruce, Jr.,
and Lloyd E. Hackman
Ribbon Technology Corporation
Gahanna, Ohio

Susan E. Brasmer and Jonathan A. Dantzig
University of Illinois
Urbana, Illinois

William A. Baeslack III
The Ohio State University
Columbus, Ohio

Prepared for
Langley Research Center
under Contract NAS1-18288



National Aeronautics and
Space Administration
Office of Management
Scientific and Technical
Information Division

1989

Executive Summary

A promising new technique for direct casting titanium ribbons for use in honeycomb structures emerged from this project. Our research demonstrated the feasibility of direct casting Ti-6Al-4V alloy strip and Ti-14Al-21Nb alloy strip by combining plasma arc melting techniques with melt overflow rapid solidification technology.

Ribtec designed and constructed a pilot plant-scale plasma melt overflow furnace to demonstrate the feasibility of casting titanium alloy ribbons. A rotatable hearth was invented for overflowing liquid titanium from the copper hearth onto the chill block to cast strip. The rotating hearth technique proved to be superior to a tilting hearth and a patent application was filed on the invention.

Over 64 experiments were performed to cast ribbons from CP titanium, Ti-6Al-4V alloy, and Ti-14Al-21Nb alloy. Evaluation of the direct cast strip shows a martensitic microstructure in Ti-6Al-4V alloys and a fine acicular transformed structure in Ti-14Al-21Nb alloys. The solid state cooling rate was estimated at 40 C/s to 300 C/s based on microhardness measurements.

The oxygen content of the Ti-14Al-21Nb increased only 340 ppm after a single remelting. The loss of aluminum after remelting Ti-14Al-21Nb alloy was about 6% but it can be compensated for by sacrificial alloying. The aluminum and vanadium levels in Ti-6Al-4V alloy tended to fall after repeated remelting.

The plasma melt overflow furnace is limited by melting capacity. It is anticipated that further improvements can be made to the direct cast strip by increasing melting capacity; by increasing the solid state cooling rate of the strip through belts, rolls, or forced convection cooling; by sacrificial alloying to maintain alloy chemistry levels; by working and conditioning the strip after casting; and by refining the hearth design and operation.

Introduction

This contract was awarded under Phase II of the NASA Small Business Innovation Research (SBIR) Program. The Phase I SBIR research program, entitled "Rapid Solidification of Low Density Alloys by Melt Overflow" (NASA Contract NAS1-17978), successfully demonstrated the feasibility of casting rapidly solidified aluminum alloys, magnesium alloys, and titanium alloys by the melt overflow process in a series of laboratory-scale experiments. The Phase II project focused on the melting of titanium alloys and casting them into strip.

Ribtec's melt overflow process involves the transfer of liquid metals and alloys from a molten reservoir onto the surface of a rotating chill block (Figure 1). Unlike conventional melt spinning techniques, the melt is not extruded through an orifice; rather, the molten material flows over a solid surface from a molten reservoir until it comes in contact with a moving chill surface. Rapidly solidified foils, fibers, flakes, filaments, strips, and particles are among the products that can be cast directly by melt overflow. In general, the final product form depends on the geometry of the casting surface.

The Phase II project objective was to demonstrate the feasibility of casting 5 cm (2 in) wide titanium alloy strip suitable for use in honeycomb structures. Continuous strips 2.4 m (8 ft) long and 0.125 mm (0.005 in) thick were requested. In order to demonstrate the feasibility of casting titanium alloy strip by melt overflow, a pilot-plant furnace was designed and constructed. Titanium alloys were melted by transferred plasma arc skull melting techniques under inert atmosphere.

The Phase II research project was organized into seven different tasks. These seven tasks were:

- Task 1 - Design/Physical Modeling
- Task 2 - Mathematical Modeling
- Task 3 - Evaluate Plasma Arc Melting
- Task 4 - Construct Plasma Melt Overflow System
- Task 5 - Processing Experiments
- Task 6 - Microstructural Evaluation
- Task 7 - Process Evaluation

Each task will be reviewed separately.

Design/Physical Modeling

Ribtec's original concept for direct casting titanium alloy strip combined transferred plasma arc melting with melt overflow casting. Titanium alloys were melted in a water-cooled copper

hearth. The liquid titanium solidified against the inner wall of the hearth to form a skull in which the liquid reservoir was contained. All melting was performed at atmospheric pressure in an inert environment.

The plasma was created by ionizing a gas in an electric arc that was established between the torch and the melt pool. The gases used for melting titanium were argon and helium. The plasma arc stream consisted of ions, electrons, and superheated gas molecules which could reach temperatures of 10,000°C or greater. The plasma torch needed to be manipulated to distribute the heat across a large surface for melting.

In combining plasma melting techniques with the melt overflow casting process, a novel system was invented for rotating the copper hearth about the chill block to achieve melt overflow. A U.S. patent application has been filed on the invention.

The plasma melt overflow system was physically modeled during experiments to cast lead in air on a copper chill block. We used an oxygen-acetylene torch for melting. Several different ribbon collection systems that employed continuous stainless steel belts or steel rolls for directing the strip were evaluated.

A book of drawings of the plasma melt overflow furnace was delivered to NASA with the Interim Report dated July 30, 1987. The detailed design of the plasma melt overflow system involved several different subsystems: electrical, hydraulic, water cooling, environmental, plasma skull melting, and melt overflow casting.

Figure 2 shows a drawing of the plasma melt overflow furnace (from Ribtec assembly drawing No. 202-A-001) designed and constructed under this contract. The plasma melt overflow unit was designed for flexibility in conducting the processing experiments. The front door of the process chamber opened to expose a steel rack. The rack could be fully extended and carried a one-ton load. The water-cooled copper hearth and chill block assembly were mounted on the rack. Full extension of the rack allowed the easier removal of the hearth and chill block. Most maintenance was performed outside the process chamber.

The plasma torch was mounted on a ball on the top of the furnace. The torch was manipulated in the X-Y and Z axes using hydraulic actuators. A crane operated over the furnace for removal of the plasma torch, chill block, hearth, or other massive components. The bottom door of the vessel opened to remove the cast strip.

The three-piece hearth was composed of a water-cooled lip and two-piece melting cavity. The lips and inserts were machined from copper blocks and attached to the hearth. This allowed us to examine different lip geometries during the processing experiments.

The furnace design allowed for expansion of the furnace capabilities. These expanded capabilities may include, but are not limited to, the following:

- a meltstock feed system
- additional viewports
- automated ribbon collection
- additional melting capability

Mathematical Modeling

A mathematical model of the plasma melt overflow process was developed at the University of Illinois by Susan Brasmer and Professor Jonathan Dantzig. The model uses a commercial finite element code FIDAP run on a Sun 3/280 computer with some additional work done on a Silcon Graphics Iris 3020 work station.

The solution process consisted of four major sections. First, a velocity solution was obtained, assuming constant temperature and a fixed ribbon thickness. This solution was then used as an initial estimate for the next solution, where the temperatures were assumed constant, but the ribbon thickness was computed. Next, the first solution was used as an initial estimate for an advection-diffusion solution to a thermal problem to obtain an estimate for the temperature field. Finally, the advection-diffusion solution and the free surface solution were used as a starting point for the fully coupled velocity and temperature solutions. Laminar flow of the fluid was assumed throughout the solution process. Each section of the solution procedure and results are described in detail in Susan Brasmer's thesis presented in Appendix A.

The model solutions found that the viscosity of the liquid titanium and the velocity of the rotating chill wheel have the greatest influence on the velocity profile in the melt and the thickness of the resulting ribbon. Surface tension and the material depth on the pouring lip also influenced the velocity solutions.

The chill wheel velocity affected the thickness of the ribbon in much the same manner as viscosity. For a constant viscosity, a high velocity value created a thin ribbon and decreasing the velocity increased the ribbon thickness. The similarity in the effects of viscosity and velocity makes sense

when one realizes that when the governing equations are non-dimensionalized, the parameter which appears is the capillary number, $Ca = \mu U / \sigma$, where:

Ca	[=]	Capillary Number
μ	[=]	Viscosity
U	[=]	Casting Speed
σ	[=]	Surface Tension

The effect of capillary number on ribbon thickness is shown in Figure 3. Increasing velocity or viscosity increased the capillary number and resulted in a thinner ribbon. Similarly, decreasing surface tension increased the capillary number and also resulted in a thinner ribbon.

The location and intensity of the torch also influenced the solidification of the ribbon. Raising the intensity or moving the torch closer to the ribbon raised the temperature of the melt in the ribbon and delayed solidification. The torch was modeled as a Gaussian distribution with a power of 75 kW.

The results indicate that the thickness of the ribbon is dependent on the capillary number of the fluid and is determined by the shape of the meniscus before the ribbon solidifies. Results from the model indicate that the most practical way to change ribbon thickness is to change the velocity of the chill block since both viscosity and surface tension, the other factors that determine the capillary number, are difficult to change for a given material.

Plasma Arc Melting

The titanium alloys were melted in a water-cooled copper hearth using a transferred plasma arc. The goal of the plasma melting experiments was to produce a 2.25 kg (5 lb) melt pool suitable for casting strip by melt overflow.

Successful operation of the plasma arc melting system presented the greatest challenge in successful completion of the research project. Numerous hardware problems were encountered in all components: the DC power supplies; the control console; the plasma torch; and the water-cooled copper hearth. Solutions were found for each of these problems, allowing titanium strip to be cast by melt overflow.

The control circuits of the DC power supplies were not properly wired resulting in one power supply providing maximum output while the second power supply provided minimum output. Combining the outputs of both power supplies, in series or in parallel, resulted in large current fluctuations and unsteady

torch operation. After the control circuits were rewired, we were able to obtain power to melt sufficient quantities of titanium to cast into strip.

The operation of the hollow anode plasma torches has been disappointing in that we have never achieved a 2.25 kg (5 lb) titanium melt pool for casting strip. Our first experiments used an argon plasma and produced a small volume of liquid titanium, roughly 10 cm (4 in) diameter and 1 cm (0.4 in) deep. We switched from an argon plasma to a helium plasma to achieve a larger melt pool.

The thermal conductivity of helium is an order of magnitude greater than the thermal conductivity of argon at room temperature, and it increases faster with increasing temperature. The voltage of a helium plasma is 25% to 50% higher than for argon plasma at comparable stand-off distances. This increases the energy available for melting. Power levels of 70 kVA to 100 kVA were typical for helium plasma melting experiments. The use of a pure helium plasma increased the size of the melt pool to roughly 17.5 cm (7 in) diameter by 1 cm (0.4) deep which represents approximately 1.2 kg (2.5 lb) of liquid titanium. The 1.2 kg (2.5 lb) melt capacity limits the width of the cast strip to approximately 5 cm (2 in) maximum if a significant length of strip is to be cast.

The water-cooled copper hearth that was delivered from the manufacturer was unsuitable for use with melt overflow. We redesigned the hearth, making it 10 cm (4 in) shorter and completely changed the lip geometry. The design that worked best used a U-shaped copper block at the front of the hearth. Heat extracting copper inserts were bolted into the U-shaped slot to reduce the width of the slot. Liquid titanium overflowed the slot to cast strip.

We monitored the water temperature in the plasma torch, copper hearth, and in a water-cooled copper chill block during experiments to cast Ti-6Al-4V alloy strip. The measurements were made with Type K thermocouples recorded on a Burr Brown PCI 20,000 Data Acquisition System installed in a personal computer. The water temperature was plotted as a function of time for the plasma torch and hearth (Figure 4). The temperature of the cooling water in the plasma torch jumped 20°C after the arc was initiated, indicating that a significant amount of I^2R heat was dissipated in the torch. The cooling water temperature increased more gradually above 40°C, probably due to radiation heat transfer from the titanium melt pool. The cooling water temperature in the torch plummeted from 45°C to 22°C after the torch current was turned off. The hearth cooling water temperature increased linearly with a 6°C total increase recorded during the experiment.

Construct Plasma Melt Overflow System

The components of the plasma melt overflow system were integrated and assembled at Ribtec in a laboratory dedicated to the production of titanium and other advanced materials. A photograph of assembled plasma melt overflow furnace is shown in Figure 5. The construction of the plasma melt overflow furnace was completed in February 1988.

The integration of the different system components resulted in the following furnace operating procedure:

1. Clean tundish (anode of plasma circuit) and ensure adequate electrical continuity between tundish and negative side leads.
2. Check chill block rotation, tundish tilting mechanism, and other mechanicals. Check torch nozzle for obstructions. Check cooling water flow, hydraulics, and vacuum pumps.
3. Add melting charge to tundish.
4. Position torch tip 0.25 to 0.50 in (0.635 cm to 1.270 cm) from melt charge.
5. Seal and evacuate chamber.
6. When pressure in chamber has reached the desired vacuum, about 30 to 35 microns of Hg, turn off vacuum pumps.
7. Turn on gas (Ar) supply and vent chamber with argon to atmospheric pressure.
8. Turn on torch helium gas supply and regulate the plasma gas flow and pressure for arc start. The pressure and flow rates are 30 psi and 8 scfm, respectively, for helium plasma.
9. Turn on water, hydraulics, and main torch power supply. Make visual check of all interlocks for safety.
10. Check open circuit voltage on main torch power supply.
11. Depress arc start button which automatically initiates pilot arc then transfers arc to the water-cooled hearth.

12. Reset torch gas flow and pressure to match manufacturer's current setting.
13. Start chill block rotation and melt charge.
14. When a sufficiently large melt pool is achieved, tip tundish and raise torch simultaneously without extinguishing arc to cast strip material.
15. Extinguish plasma torch arc and turn off plasma gas supply.
16. Evacuate the chamber.
17. Open chamber and remove skull and cast material.

Processing Experiments

Sixty-four (64) experiments were performed to direct cast titanium strip in the plasma melt overflow furnace. Ti-6Al-4V alloy, Ti-14Al-21Nb alloy, and CP titanium were cast into strip. All of the casting experiments were performed on a knurled molybdenum solid substrate. Experiments performed at Ribtec have shown that molybdenum is an excellent substrate for casting both Ti-6Al-4V alloy and Ti-14Al-21Nb alloy. A pure helium plasma was used for melting the titanium alloys.

Table I presents the physical dimensions of the strip cast, the alloy compositions, and the casting speed. The width and length of strip cast by plasma melt overflow appear to be suitable for use in honeycomb structures. However, the thickness of the cast strip varies from experiment to experiment and across the length and width of the strip for a single experiment.

The process parameters that appear to have the greatest influence on the width of the cast strip are the crucible skull thickness, the hearth pour rate, the substrate speed and surface condition, and the physical properties of the liquid (viscosity and surface tension). Variations in the skull thickness at the pouring lip produces variations in melt depth against the chill block. In extreme cases, the liquid will solidify against the side walls of the pouring lip, thereby reducing the width of cast strip. The pour rate must be fast enough to supply liquid to completely fill the pour lip in order to cast full width strip. Defects on the substrate surface or excessive casting speed can result in narrowing of the cast strip. These effects are governed by the physical properties of the liquid being cast.

The process parameters that appear to have the greatest influence on the thickness of the cast strip are the casting speed, the depth of liquid in contact with the substrate, and the physical properties of the liquid (viscosity and surface tension). Two factors that influence the melt depth are the rate at which the hearth rotates about the chill block to overflow the liquid titanium on the moving substrate and the amount of superheat of the liquid. The tilt of the hearth is constant during each experiment but the volume of liquid being poured can vary depending on the geometry of the hearth and skull. The superheat varies from the liquidus temperature at the skull interface to the maximum temperature at the region the plasma arc stream contacts the surface.

The mean thickness of the as-cast plasma melt overflow strip is plotted against capillary number in Figure 6. The capillary number is a dimensionless parameter which takes the viscosity (μ), surface energy (σ), and casting speed (U) into account. Figure 6 also presents the computed thicknesses from the mathematical model developed at the University of Illinois. The curves represent "best-fit" power series of the computed and experimental values. If the mathematical model is valid, the depth of liquid in contact with the chill block is less than 4 mm. If the experimental data are fitted to the power series $t = 270.557 + 2001.682 \exp(-250 Ca)$, it suggests a melt depth of 1 mm.

The mathematical model agrees quite closely with the experimental data. There are few as-cast strip thickness values that fall below the zero depth curve in Figure 6. The model predicted slightly thicker titanium strip than was achieved experimentally, but the experimental values generally fall within the range calculated by the model.

The depth of liquid in contact with the rotating chill block was not measured; therefore, we cannot compare the melt depth to those predicted by the mathematical model in Figure 6. We are not aware of any noncontacting technique for measuring the depth of the liquid titanium. Immersible probes may be used to measure melt depth with the risk of contamination of the titanium melt pool. If the immersed probe is heat extracting, the precision of the measurement would be low because of skull formation on the probe itself. If the level of the liquid changes with time, several probes would need to be immersed in sequence. The mathematical model was, therefore, useful in estimating values where measurements are difficult or impossible to make.

Experiments were also performed to cast Ti-6Al-4V alloy strip on a water-cooled copper chill block. Figure 7 shows the temperature of the cooling water in the plasma torch and in the water-cooled chill block. The torch was turned off immediately after casting Ti-6Al-4V alloy strip. The temperature of the

chill block cooling water "spikes" about 10°C, 8 to 10 seconds after the casting takes place. The delay reflects the time required for conduction heat transfer from the solidified strip to the copper substrate and for convection heat transfer from the chill block to the cooling water.

Microstructural Evaluation

Specimens were cut from as-cast Ti-6Al-4V alloy strip and Ti-14Al-21Nb alloy strip cast by melt overflow. The specimens were mounted in thermosetting resin, ground, polished, and etched to reveal the microstructure. The etchant used with Ti-6Al-4V alloy strip was 95% H₂O + 3.5% HNO₃ + 1.5% HCl. The etchant used with the Ti-14Al-21Nb alloy strip was 0.5% HF + 1.5% HCl + 2.5% HNO₃ + 95.5% H₂O (Keller's Reagent). The specimens were examined under a light microscope using differential interference-contrast (Nomarski) illumination.

Figure 8 presents photomicrographs of the top and bottom surfaces of as-cast Ti-6Al-4V alloy strip. Figure 9 presents photomicrographs of the transverse and longitudinal cross sections of the as-cast Ti-6Al-4V alloy strip. Solidification begins at the substrate and grows radially outward into the melt from the chill block surface. The strip exhibits elongated, columnar beta grains in the longitudinal (Figure 9A) and transverse (Figure 9B) directions. The strip surface that contacted the substrate (Figure 8A) shows relatively equiaxed beta grains. Equiaxed beta grains are also found on the free surface of the cast strip (Figure 8C).

After solidification, the Ti-6Al-4V alloy strip underwent a martensite transformation. Areas of grain boundary alpha (Figure 8B) can be found along with the fine alpha-prime platelets inside the beta grains. The presence of grain boundary alpha indicates that solid state cooling is slow enough to allow alpha to form at the grain boundaries.

The microstructure of the as-cast Ti-14Al-21Nb (alpha-two) strip is presented in Figure 10. The microstructure also consists of elongated, nearly columnar beta grains which appear equiaxed on the substrate surface (Figure 10A) and the top surface (Figure 10C) of the strip with a cellular-dendritic solidification substructure within these grains. Higher magnification (Figures 10B, 10D) reveals an acicular transformed structure that is probably alpha-two or ordered alpha prime martensite. Further study by use of analytical microscopy techniques is needed to distinguish the phases present in the transformed structure. There may be variations in this transformed structure resulting from compositional variations due to segregation during solidification.

In comparing the substrate surface to the free surface of the as-cast Ti-14Al-21Nb alloy strip, it appears that the cellular dendritic substructure is coarser on the free-cast surface, reflecting a slightly lower cooling rate.

Process Evaluation

The titanium alloy strip direct cast by plasma melt overflow was further characterized by chemical analysis, microhardness measurements, and cold rolling.

Chemical Analysis - The results of chemical analysis of the Ti-6Al-4V alloy strip are presented in Table II. In general, blocks of Ti-6Al-4V alloy billets were initially melted to create a skull from which strip was cast. After casting, the skull was remelted again and again with Ti-6Al-4V alloy scrap used to replenish the liquid level. Therefore, the chemical composition of the strip combines the compositions of the original Ti-6Al-4V alloy billet and Ti-6Al-4V alloy scrap. The "starter material" shown in Table II is Ti-6Al-4V alloy scrap taken from a random sample. The intent was to compare the chemical compositions of the starting scrap with the final strip to estimate the level of contamination from remelting in the plasma furnace recognizing that there may be variations in the chemical composition of the starting materials.

Table II compares the chemistry of strip cast from Ti-6Al-4V alloy billet (Experiment 36) with strip cast from a skull that had been remelted several times (Experiment 60). In general, the levels of interstitial elements increase as the skull is melted more often while the aluminum and vanadium levels decrease with more frequent remelting.

The Ti-14Al-21Nb (alpha-two) alloy was melted from pre-alloyed plate purchased from Timet. The chemical analysis of the plate is compared to that of the strip in Table III. Note that the analyses of the plate and strip were performed at different laboratories. The most striking result is a 6% depletion of aluminum from the melt which causes the niobium content to rise relative to the other elements. However, aluminum has the lowest boiling point of the three major alloying elements - 2450°C compared to 3260°C for titanium and 3300°C for niobium. We can compensate for the loss of aluminum by alloying.

Based on the results presented in Table III, the oxygen content of the Ti-14Al-21Nb alloy strip increased by 340 ppm after remelting and casting. The increases in other interstitial elements included carbon - 20 ppm; hydrogen - 12 ppm; and nitrogen - 40 ppm. These low values of interstitial elements indicate that the plasma melt overflow furnace and skull melting

procedures can effectively limit the interstitial contamination of titanium alloys during direct strip casting.

Microhardness - The microhardness of as-cast Ti-14Al-21Nb (alpha-two) strip was measured using a diamond point indenter with a 500 gram load. Eight (8) measurements were taken across a cross section of strip. The mean microhardness was 490 on the Vickers scale with a standard deviation of 13. Researchers at The Ohio State University [1] plotted microhardness as a function of cooling rate showing a comparison of CCT samples with simulated gas tungsten arc (GTA) fusion and heat affected zone specimens for a Ti-14Al-21Nb alloy (Figure 11). A Vickers hardness of 490 intersects the curve presented in Figure 11 at a cooling rate of 40 C/s and again at 300 C/s.

A continuous cooling transformation (CCT) diagram for the Ti-14Al-21Nb alloy is shown in Figure 12 [1]. The diagram indicates that the beta phase will be present in samples cooled at rates below 5° C/s and above 600 C/s. There is no evidence of the beta phase in the microstructure of the as-cast Ti-14Al-21Nb alloy strip (Figure 10). Further microstructural analysis using thin foil transmission electron microscopy (TEM) would allow us to estimate the cooling rate more precisely. So, we conclude that the solid state cooling rate is in the range of 40 C/s to 300 C/s.

Cold Rolling - Surface roughness of the as-cast strip can be effectively reduced by cold rolling. Twenty-one percent (21%) cold rolling did not induce significant cracking and produced a relatively smooth surface.

Variations in the thickness of the as-cast Ti-6Al-4V alloy be reduced by cold rolling. Thickness variations on the order of $\pm 20\%$ are common for as-cast strip. After cold rolling, the thickness variation was reduced to roughly $\pm 6\%$ longitudinally. These results are encouraging; however, further investigation is needed to optimize the thermomechanical processing of cast titanium alloy strip.

The micrographs presented in Figure 13 show a representative transverse cross section and longitudinal cross section of cold rolled Ti-6Al-4V strip. It appears that the martensitic structure is beginning to be broken up after 21% cold reduction. In the transverse section (Figure 13A), the free-cast surface appears to be deformed more than the chill-cast surface because of the variation in thickness on the free-cast surface of the strip.

Figure 13B shows a representative longitudinal cross section of Ti-6Al-4V alloy strip after 21% cold reduction. Shear bands are clearly evident across the longitudinal thickness of the strip. The strip is most heavily deformed along its length

during cold rolling while deformation across the width results from thickness variations.

Conclusions

- Direct casting of titanium alloy strip is feasible by combining transferred plasma arc melting techniques with melt overflow rapid solidification technology.
- The pilot plant-scale plasma melt overflow system constructed during this contract is limited by melting capacity. It is estimated that the 75 kW transferred plasma arc system melts about 1.2 kg (2.5 lb) of titanium per experiment.
- A rotatable water-cooled hearth was invented for overflowing the liquid titanium onto the chill block. This invention is a significant improvement over a tilting hearth. A U.S. patent application was filed on the invention.
- A mathematical model of the plasma melt overflow was developed to predict ribbon thickness as a function of casting speed (capillary number). The ribbon thicknesses calculated from the model are close to the thicknesses measured from as-cast strip, erring slightly on the high side. Both calculated and empirical data suggest it is possible to cast titanium strip 0.125 mm (0.005 in) thick.
- The rotatable hearth system is capable of casting titanium alloy strip of a suitable width and length for use in honeycomb structures. However, there are variations in thickness of the strip, both across the length and width of each strip sample and from sample to sample.
- The level of interstitial contaminants increases as the titanium alloys are remelted over and over while the aluminum and vanadium levels fall in the Ti-6Al-4V alloy. Aluminum depletion was particularly severe in the Ti-14Al-21Nb alloy. Sacrificial alloying can be used to compensate for unrecoverable losses during plasma melting.
- The microstructure of the Ti-6Al-4V alloy shows elongated beta grains normal to the chill surface with equiaxed beta at the substrate surface and free cast surface. The strip underwent a martensite transformation after solidification.
- The cooling rate of the Ti-14Al-21Nb alloy strip was estimated to range between 40 C/s and 300 C/s after solidification. The as-cast strip exhibited a fine acicular transformed microstructure. The solid state cooling rate

can be increased by decreasing the strip thickness or by increasing the heat transfer through use of belts, rollers, or forced gas convection.

- The surface roughness of Ti-6Al-4V alloy strip can be effectively removed by rolling. Other techniques, like grinding and slitting, might also be considered for conditioning the as-cast strip for use in honeycomb structures.

Recommendations

- Evaluate different hearth geometries to improve the fluid flow and temperature distribution in the melt pools.
- Reduce the variation in as-cast strip thickness. For the rotatable hearth, the thickness variations may be reduced through a variable tilt rate. A secondary roll might also be effective in reducing thickness variations.
- Increase the melting capacity by installation of a larger plasma melting system in addition to the 75 kW system already installed. The existing hearth could be replaced with a two-tier stationary hearth with melting performed in one section and strip casting in the second section. This concept appears to be feasible for strip less than 5 cm (2 in) wide.
- Investigate rolling, grinding, and/or slitting of the as-cast strip to achieve final ribbon dimensions and surface finish.
- Evaluate techniques for increasing the solid state cooling rate of the cast strip like secondary rollers, continuous belts, or forced convection cooling.
- Use sacrificial alloying to maintain aluminum and vanadium levels in alloys. Limit the number of times that the titanium skull is remelted to control the level of the interstitial contaminants.
- Investigate casting of different titanium alloys that are candidates for use in honeycomb structures.

References

1. Mascarella, T. J., "Weldability of A Ti₃Al-Nb Alloy", Master's Thesis, The Ohio State University (1987)

Table I

Dimensions of Direct Cast Titanium Strip

Exp. #	Casting Speed (m/s)	Mean Thickness		Maximum Width		Length (m)	Alloy
		(mm)	(in)	(mm)	(in)		
1	3.2	0.343	0.014	50.7	2.0	N/A*	Ti-6Al-4V
2	10.1	0.245	0.010	30.0	1.2	N/A	Ti-6Al-4V
3	N/A	0.377	0.015	92.9	3.7	N/A	Ti-6Al-4V
4	N/A	0.215	0.008	38.8	1.5	N/A	Ti-6Al-4V
5	7.6	0.337	0.013	113.2	4.5	N/A	Ti-6Al-4V
6	7.6	0.427	0.017	71.4	2.8	N/A	Ti-6Al-4V
7	7.6	0.415	0.015	113.2	4.5	N/A	Ti-6Al-4V
8	N/A	0.210	0.008	54.9	2.2	N/A	Ti-6Al-4V
9	N/A	0.302	0.012	33.7	1.3	N/A	Ti-6Al-4V
10	N/A	0.312	0.012	48.5	1.9	N/A	Ti-6Al-4V
11	N/A	0.618	0.024	48.2	1.9	N/A	Ti-6Al-4V
12	N/A	0.300	0.012	12.9	0.5	N/A	Ti-6Al-4V
13	N/A	0.410	0.016	38.1	1.5	N/A	Ti-6Al-4V
14	N/A	0.500	0.020	47.8	1.9	N/A	Ti-6Al-4V
15	N/A	0.560	0.022	45.9	1.8	N/A	Ti-6Al-4V
16	N/A	0.463	0.018	27.4	1.1	N/A	Ti-6Al-4V
17	N/A	0.340	0.013	14.5	0.6	N/A	Ti-6Al-4V
18	N/A	0.500	0.020	46.7	1.8	N/A	Ti-6Al-4V
19	8.1	0.533	0.021	18.3	0.7	1.8	Ti-6Al-4V
20	8.1	0.284	0.011	17.8	0.7	2.7	Ti-6Al-4V
21	8.1	0.310	0.012	17.5	0.7	2.7	Ti-6Al-4V
22	3.4	0.516	0.020	42.7	1.7	3.3	Ti-6Al-4V
23	3.4	0.381	0.015	29.2	1.2	2.7	Ti-6Al-4V
24	3.4	0.406	0.016	17.0	0.7	1.8	Ti-6Al-4V
25	3.4	0.381	0.015	4.5	0.2	1.8	Ti-6Al-4V
26	3.4	0.290	0.011	23.5	0.9	1.9	Ti-6Al-4V
27	4.2	0.345	0.014	40.6	1.6	3.0	Ti-6Al-4V
28	5.0	0.157	0.006	50.8	2.0	3.8	Ti-6Al-4V
29	5.0	0.345	0.014	36.8	1.5	5.1	Ti-6Al-4V
30	5.0	0.239	0.009	58.4	2.3	2.8	Ti-6Al-4V
31	5.3	0.356	0.014	37.5	1.5	3.1	Ti-6Al-4V
32	2.3	0.625	0.025	111.8	4.4	1.2	Ti-6Al-4V
33	5.3	0.385	0.015	45.7	1.8	2.0	CP Ti
34	5.3	0.254	0.010	19.1	0.8	2.1	CP Ti
35	5.3	0.305	0.012	43.2	1.7	2.3	Ti-6Al-4V
36	5.0	0.178	0.007	57.7	2.3	2.5	Ti-6Al-4V
37	3.4	0.698	0.027	55.2	2.2	0.5	Ti-6Al-4V
38	4.4	0.566	0.022	54.9	2.2	N/A	Ti-6Al-4V
39	3.4	0.930	0.037	50.8	2.0	1.0	Ti-6Al-4V
40	4.1	0.363	0.014	55.9	2.2	2.1	Ti-6Al-4V
41	4.1	0.643	0.025	35.6	1.4	1.7	Ti-6Al-4V
42	4.1	0.401	0.016	27.9	1.1	1.7	Ti-6Al-4V
43	3.8	0.413	0.019	50.8	2.0	3.0	Ti-6Al-4V
44	5.9	0.445	0.018	50.8	2.0	1.7	Ti-6Al-4V
45	3.4	0.676	0.027	101.6	4.0	3.0	Ti-6Al-4V
46	3.4	0.922	0.036	19.1	0.8	3.1	Ti-6Al-4V
47	4.2	0.500	0.020	66.7	2.6	2.4	Ti-6Al-4V
48	4.1	0.533	0.021	18.4	0.7	4.9	Ti-6Al-4V
49	4.2	0.338	0.013	66.0	2.6	2.9	Ti-6Al-4V
50	5.3	0.427	0.017	50.8	2.0	N/A	Ti-6Al-4V
51	5.3	0.203	0.008	72.1	2.8	2.4	Ti-6Al-4V
52	4.4	0.343	0.014	95.8	3.8	1.8	Ti-6Al-4V
53	4.2	0.427	0.017	98.3	3.9	2.9	Ti-6Al-4V
54	4.5	0.241	0.010	43.2	1.7	1.4	Ti-6Al-4V
55	5.7	0.211	0.008	47.6	1.9	4.7	Ti-6Al-4V
56	6.9	0.381	0.015	54.0	2.1	7.6	Ti-6Al-4V
57	7.4	0.218	0.009	43.2	1.7	3.6	Ti-6Al-4V
58	5.6	0.287	0.011	45.7	1.8	8.2	Ti-6Al-4V
59	7.4	0.170	0.007	29.2	1.2	3.8	Ti-6Al-4V
60	6.9	0.160	0.006	42.5	1.7	2.6	Ti-6Al-4V
61	5.3	0.279	0.011	48.3	1.9	3.0	Ti-14Al-21Nb
62	6.3	0.229	0.009	48.9	1.9	3.0	Ti-14Al-21Nb
63	5.3	0.406	0.016	48.9	1.9	3.0	Ti-14Al-21Nb
64	5.3	0.381	0.015	48.9	1.9	3.0	Ti-14Al-21Nb

* N/A = Not Available

Table II

Chemical Analysis of Direct Cast
Ti-6Al-4V Alloy Strip* (Wt %)

	<u>Starter Material</u>	<u>Exp. #36</u>	<u>Exp. #60</u>	<u>Method</u>
Carbon	0.02	0.03	0.04	Leco WR-12
Hydrogen	0.0055	0.0041	0.0047	Leco Hot Extraction, 534-600
Oxygen	0.185	0.209	0.259	Leco TC 136
Nitrogen	0.009	0.038	0.066	Leco TC 136
Aluminum	6.20	6.05	5.90	Beckman Spectraspan, VI D.C. Plasma
Vanadium	4.09	3.95	3.52	Beckman Spectraspan, VI D.C. Plasma

*Results from Sherry Laboratories, Muncie, Indiana, Report #L-5166

Table III

Chemical Analysis of Direct Cast
Ti-14Al-21Nb Alloy Strip (Wt %)

	<u>Plate*</u>	<u>Exp. #61**</u>	<u>Method**</u>
Carbon	0.018	0.020	Leco WR-12
Hydrogen	0.005	0.0062	Leco Hot Extraction, 534-600
Oxygen	0.050	0.084	Leco TC 136
Nitrogen	0.012	0.016	Leco TC 136
Aluminum	14.20	13.35	Beckman Spectraspan, VI D.C. Plasma
Niobium	21.30	21.70	Beckman Spectraspan, VI D.C. Plasma

* Results from Timet Certified Analysis, Heat T-8738, Test E-3755

** Results from Sherry Laboratories, Muncie, Indiana, Report #L-5167

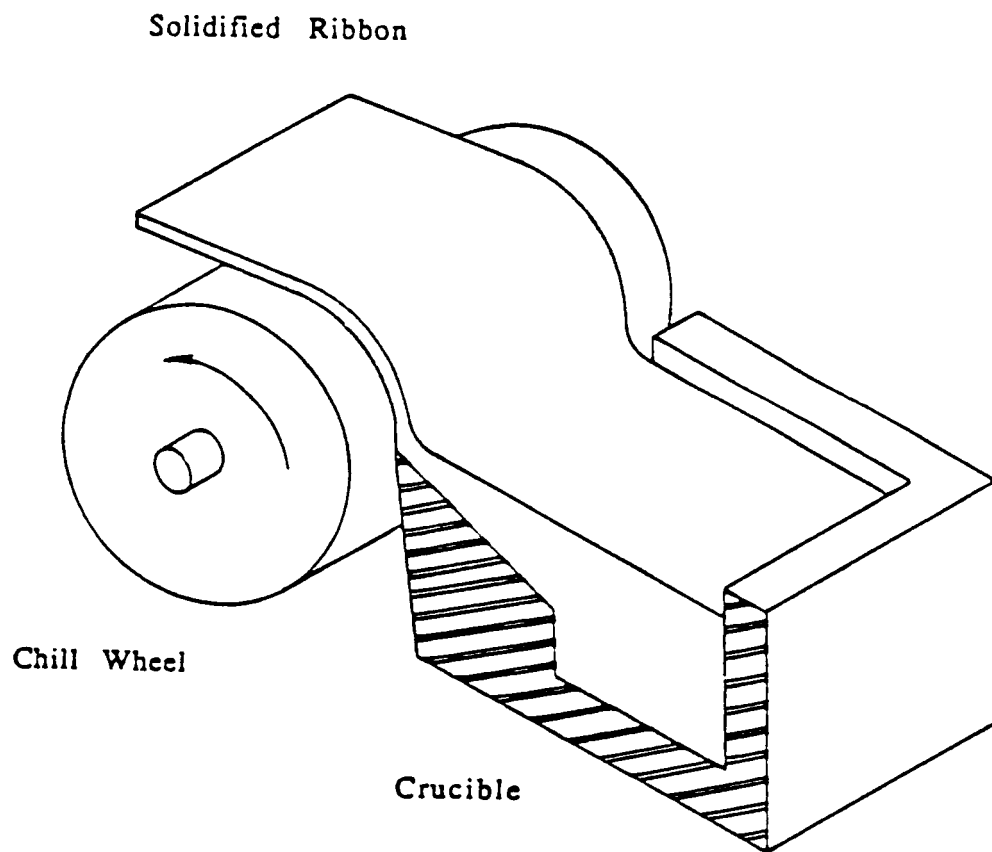


Figure 1. Schematic of the Melt Overflow Process

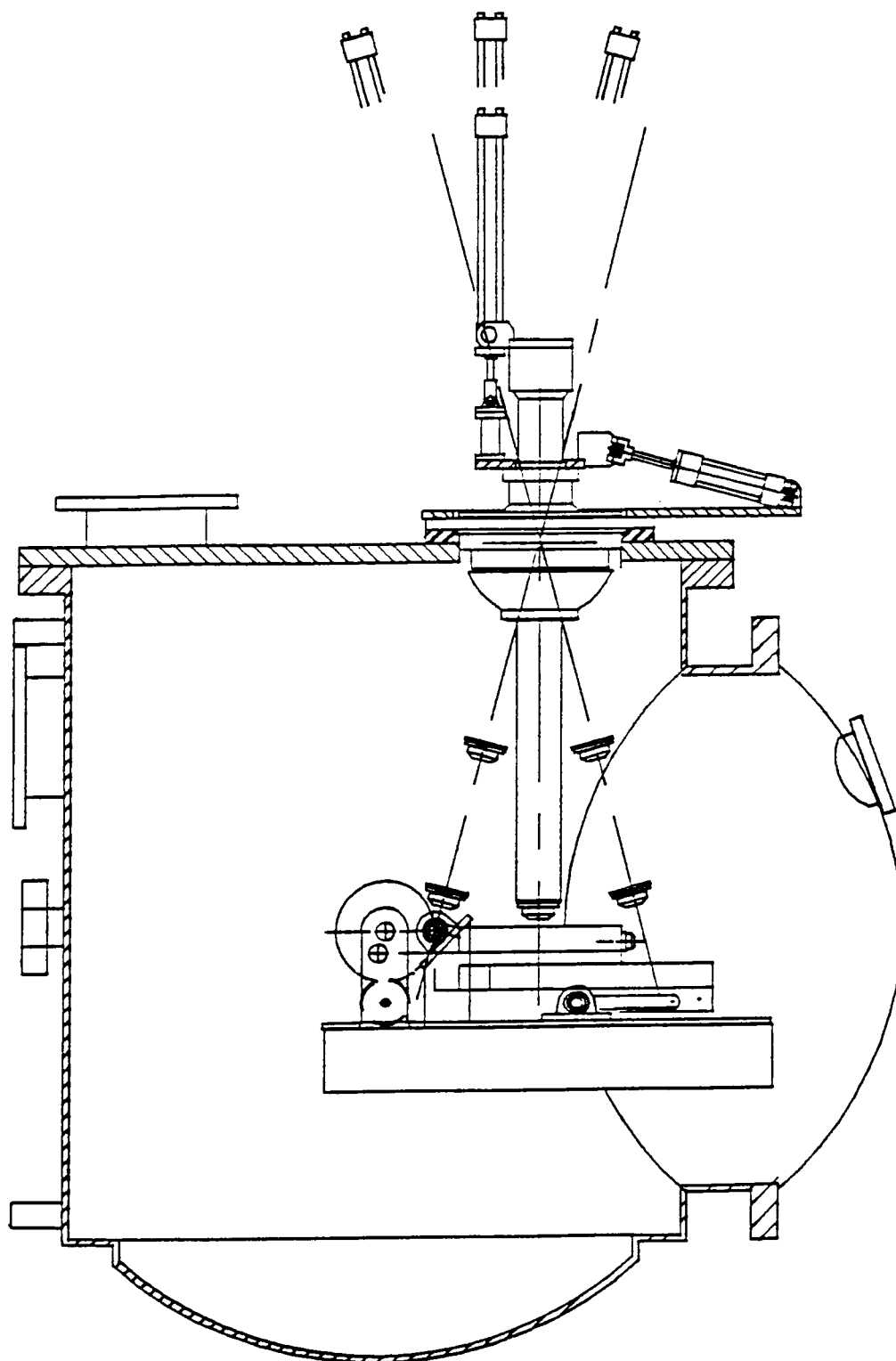


Figure 2. Schematic of Plasma Melt Overflow Furnace

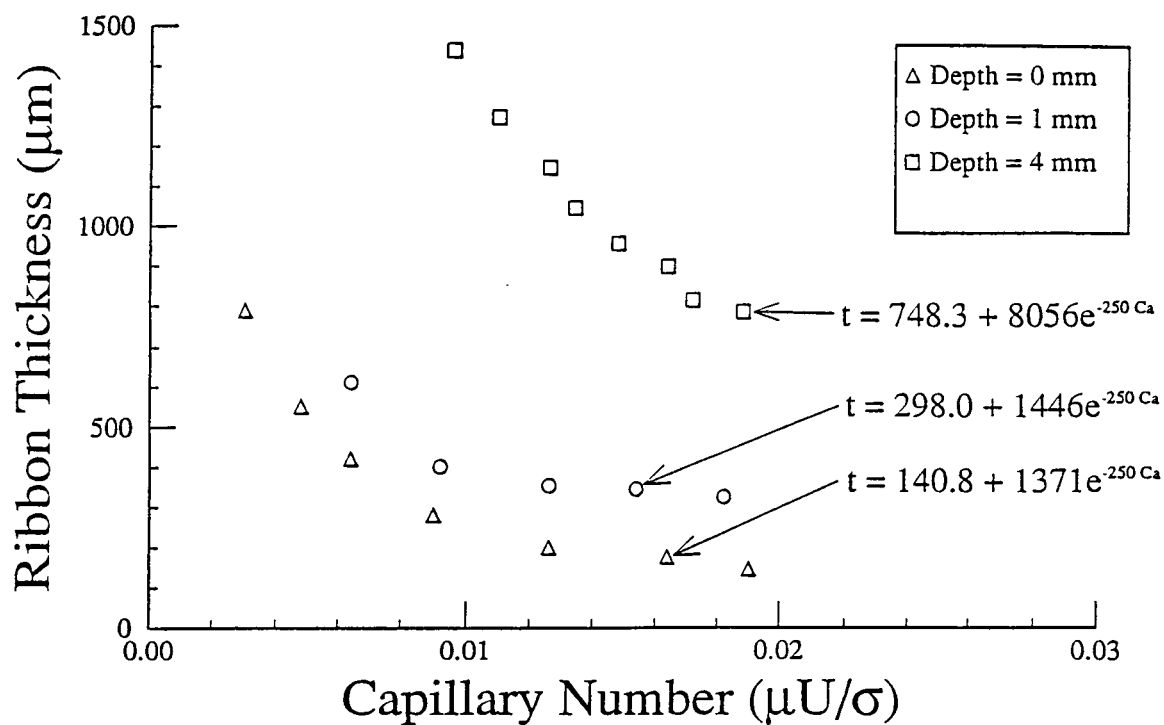


Figure 3. Computed Thickness of Titanium Strip

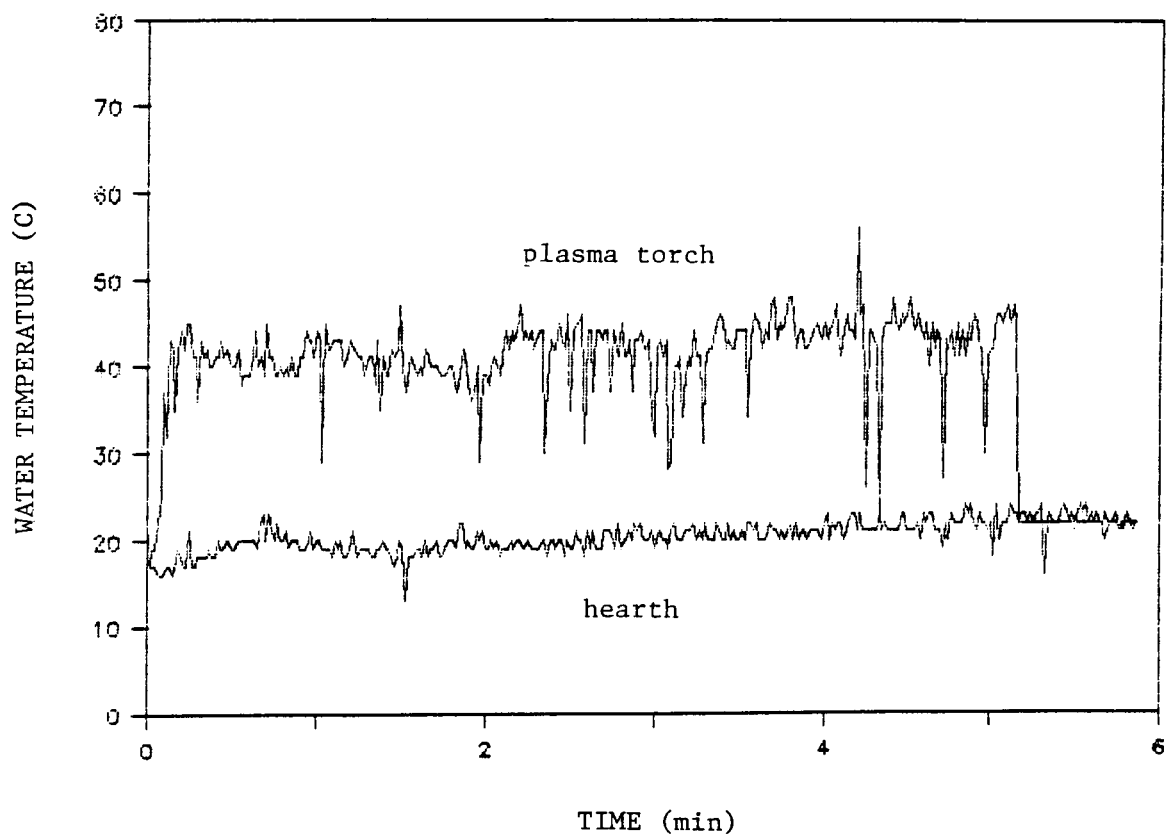


Figure 4. Water Temperature During Plasma Arc Melting

ORIGINAL PAGE
BLACK AND WHITE PHOTOGRAPH

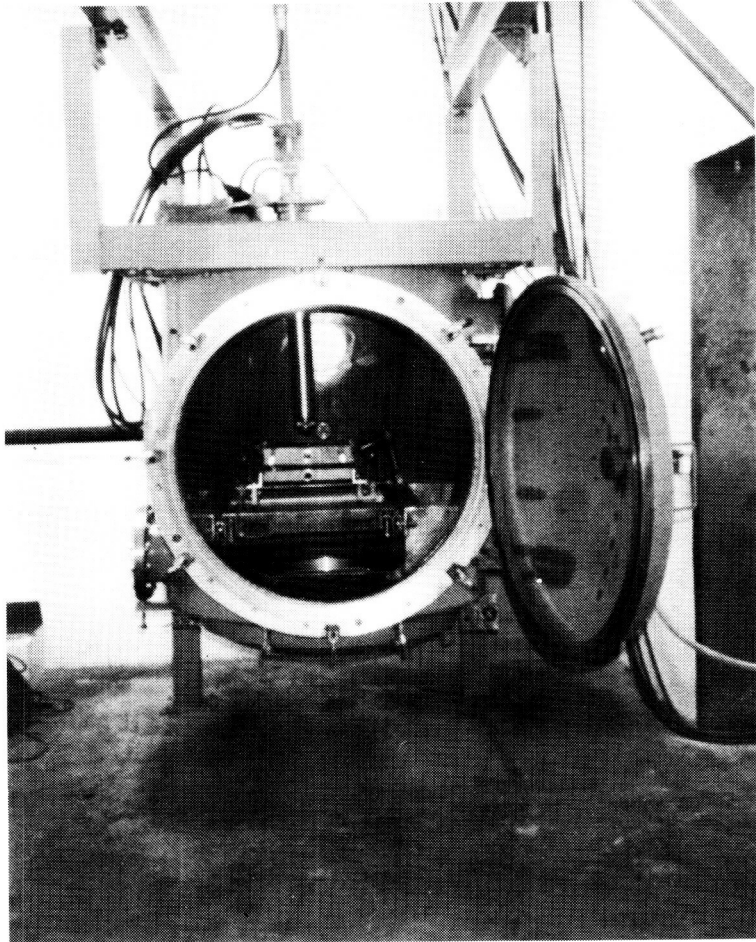


Figure 5. Photograph of Plasma Melt Overflow Furnace

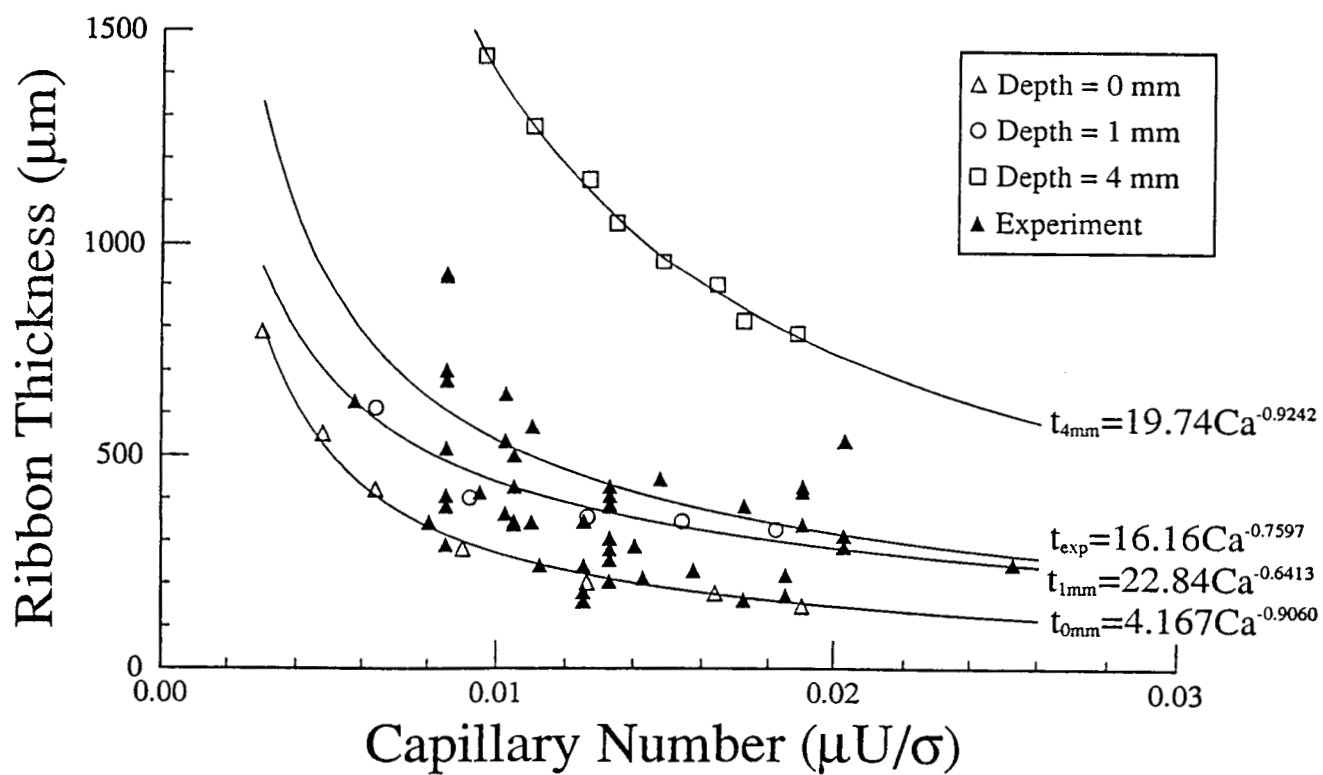


Figure 6. Computed Versus Cast Strip Thickness

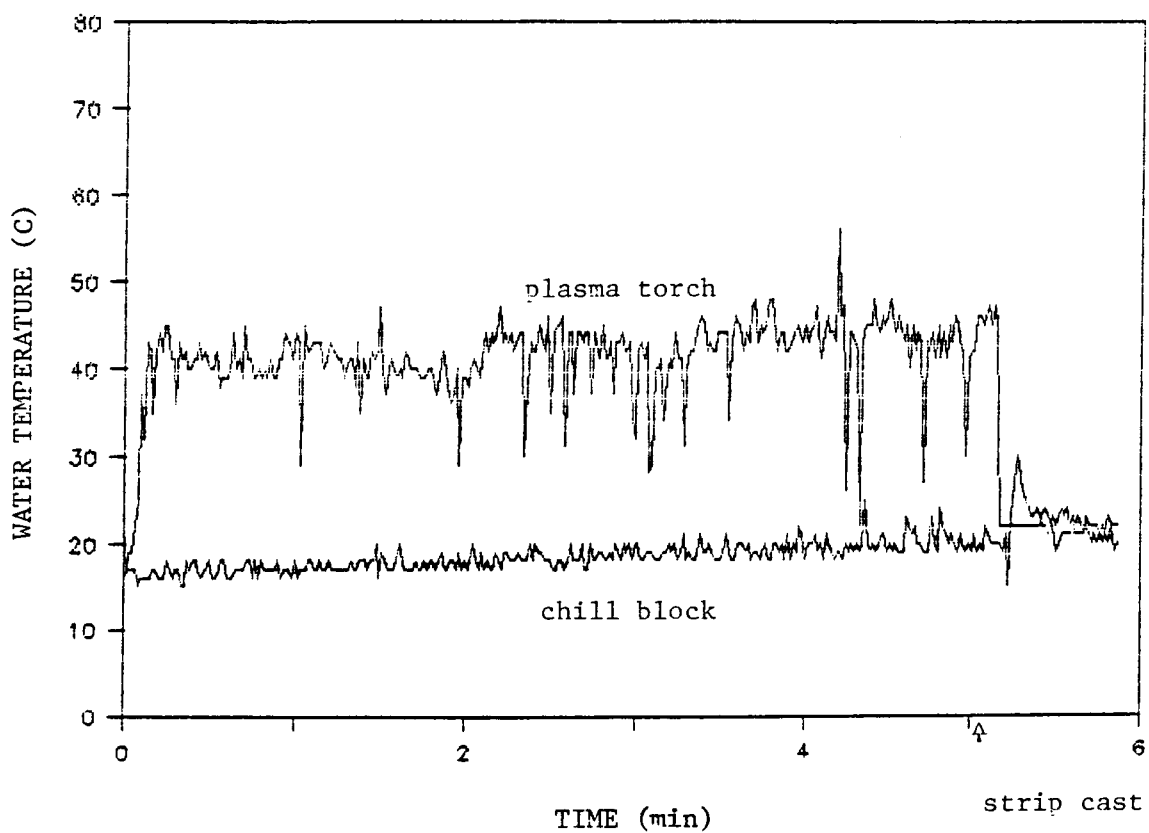


Figure 7. Water Temperature During Ti-6Al-4V Alloy Strip Casting

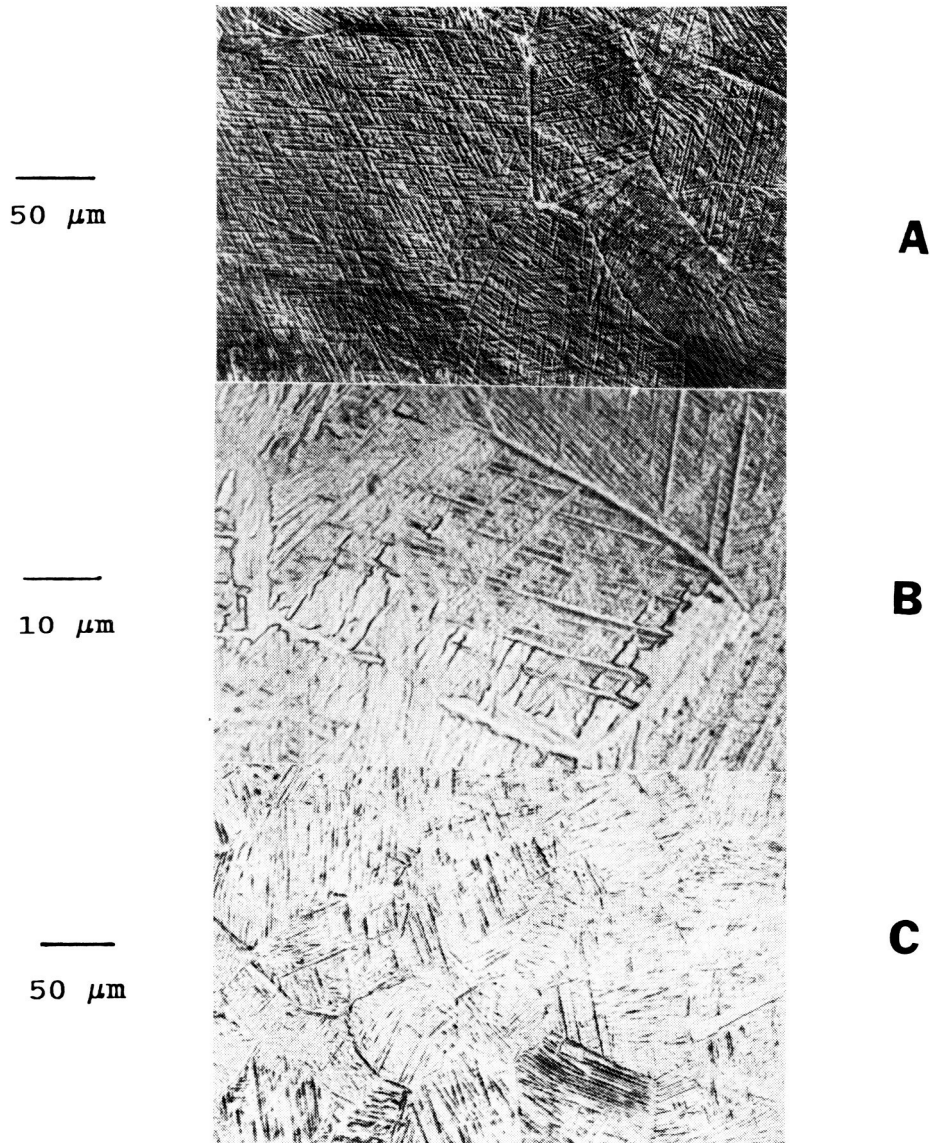
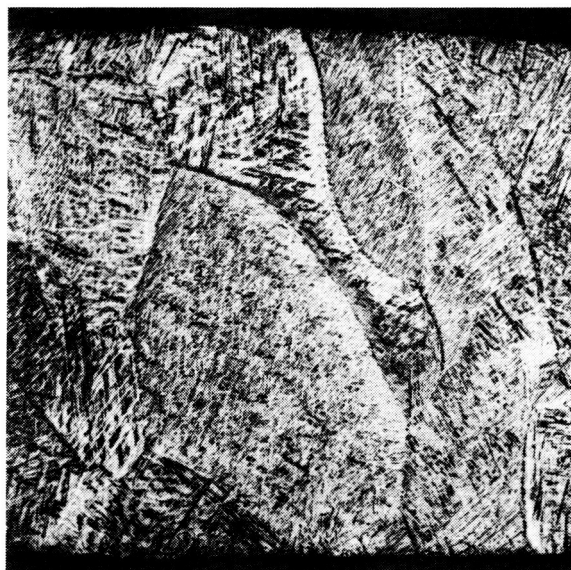


Figure 8. Microstructure of As-Cast Ti-6Al-4V Alloy Strip

- (a) Chill Cast Surface
- (b) Chill Cast Surface
- (c) Free Cast Surface

ORIGINAL PAGE
BLACK AND WHITE PHOTOGRAPH

50 μm

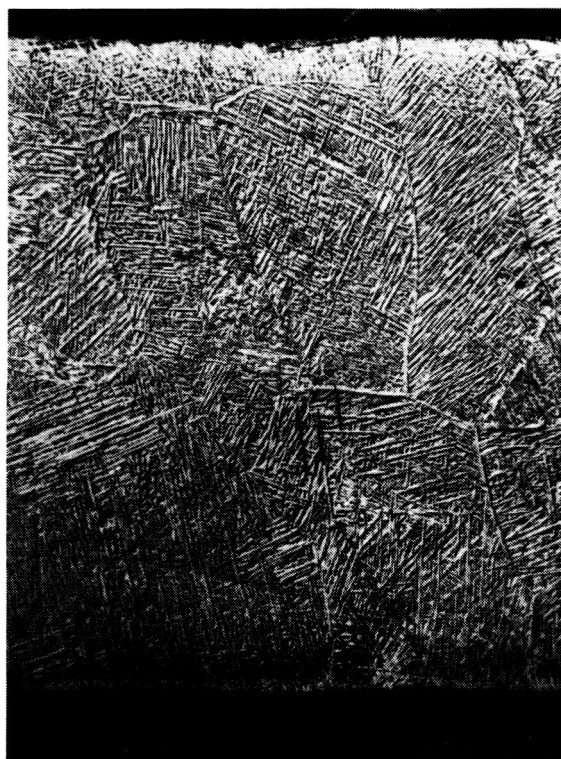


FREE
SURFACE

A

CHILL
SURFACE

50 μm



FREE
SURFACE

B

CHILL
SURFACE

Figure 9. Microstructure of As-Cast Ti-6Al-4V Alloy Strip

- (a) Longitudinal Cross Section
- (b) Transverse Cross Section

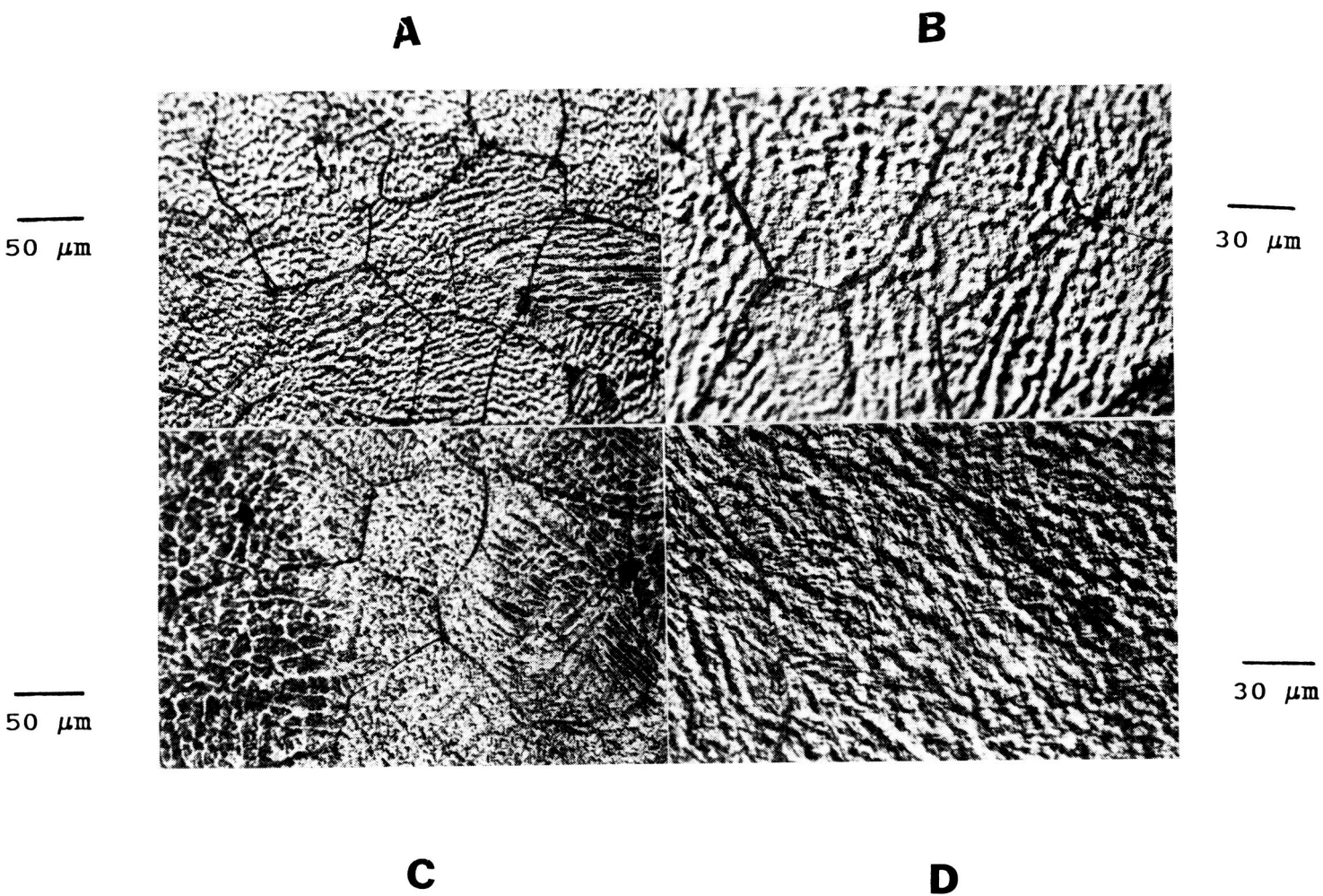


Figure 10. Microstructure of As-Cast Ti-14Al-21Nb Alloy Strip

- (a) Chill Cast Surface
- (b) Chill Cast Surface
- (c) Free Cast Surface
- (d) Free Cast Surface

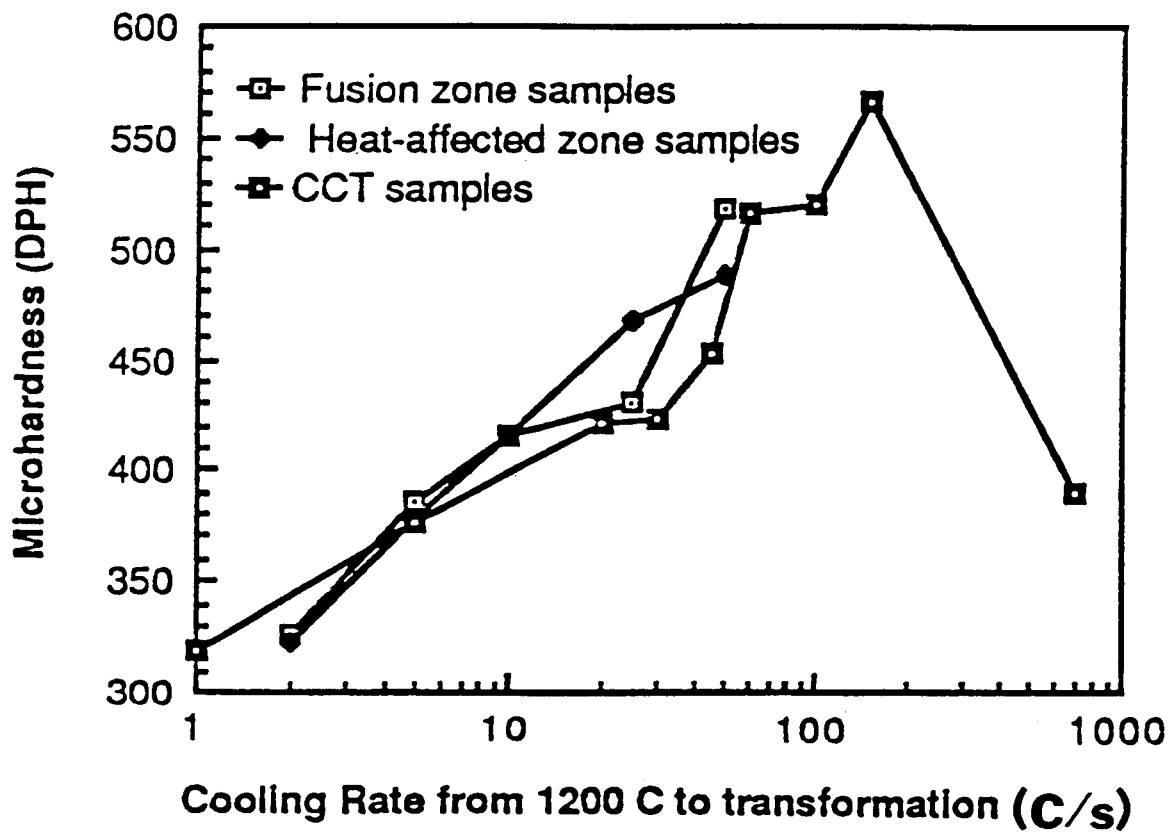


Figure 11. Graph of Microhardness as a Function of Cooling Rate for Ti-14Al-21Nb Alloy Showing Comparison of CCT Samples with Simulated GTA Fusion & Heat-Affected Zone Specimens

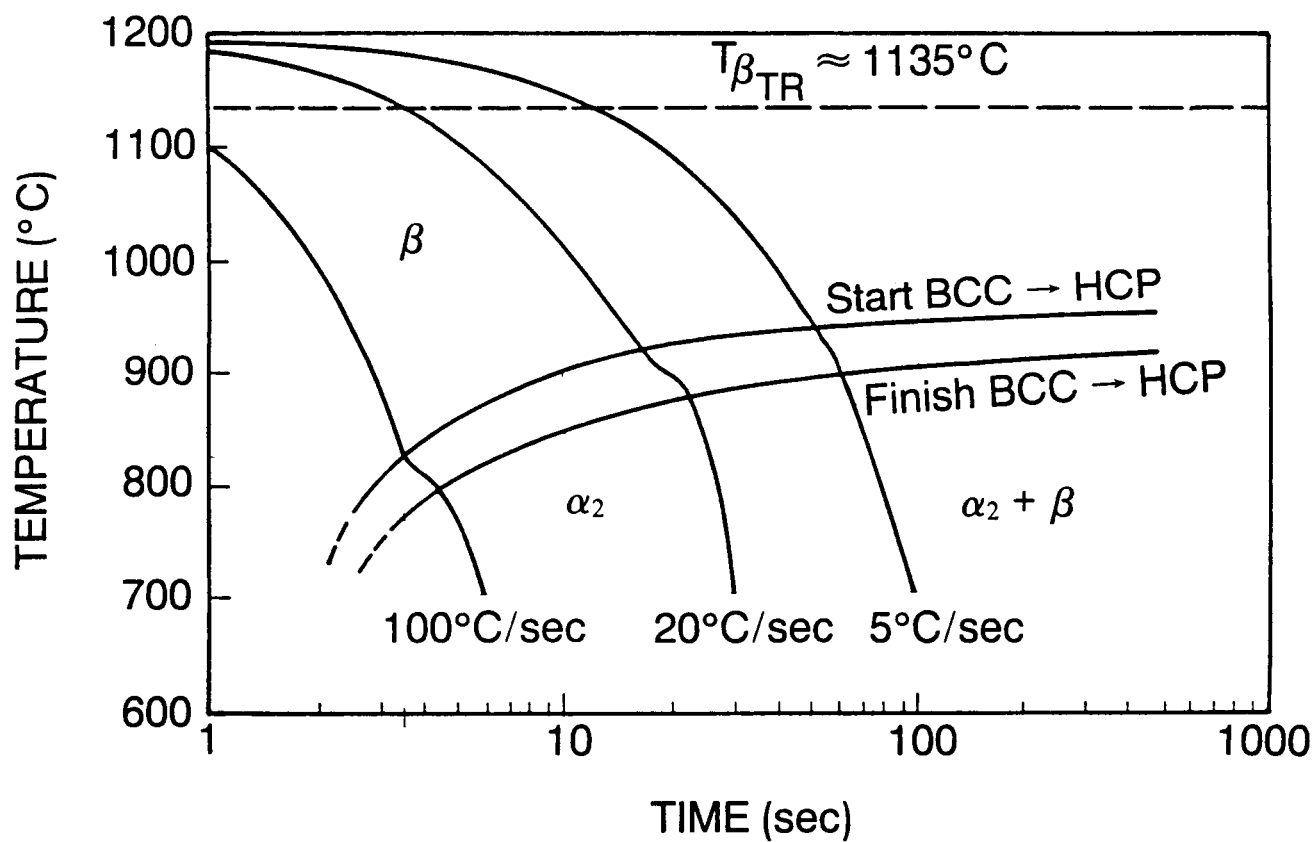


Figure 12. CCT Diagram for Ti-14Al-21Nb Alloy

ORIGINAL PAGE
BLACK AND WHITE PHOTOGRAPH

50 μm



FREE
SURFACE

A

CHILL
SURFACE

50 μm



FREE
SURFACE

B

CHILL
SURFACE

Figure 13. Micrographs of Cold Rolled Ti-6Al-4V Alloy Strip

- (a) Transverse Cross Section
- (b) Longitudinal Cross Section

APPENDIX A

A MATHEMATICAL MODEL OF THE
MELT OVERFLOW RAPID SOLIDIFICATION PROCESS

BY

SUSAN E. BRASMER

B.S., University of Illinois, 1979

THESIS

Submitted in partial fulfillment of the requirements
for the degree of Master of Science in Mechanical Engineering
in the Graduate College of the
University of Illinois at Urbana-Champaign, 1988

Urbana, Illinois

PRECEDING PAGE BLANK NOT FILMED

A-2 ~~PRECEDING PAGE BLANK NOT FILMED~~

Abstract

The melt overflow solidification process is a method for producing a thin, continuous ribbon of rapidly solidified metal with unique strength, magnetic, and corrosion properties. The process being studied was developed in 1983 by the Ribbon Technology Corporation (Ribtec) of Gahanna, Ohio [1]. The material produced with this process may be used in place of rolled strip for honeycomb and similar aerospace structural applications. A finite element model of this process has been created to study the factors that influence the formation of the ribbon and to suggest improvements to the manufacturing process. While the process is applicable to a number of alloys, including aluminum, magnesium, titanium, nickel, and copper, this work has focused on titanium.

Acknowledgements

I would first like to thank Professor Jon Dantzig for all his advice and support during the course of this project. With his guidance, I learned not only to "guess the answer", but also how to prove or disprove the accuracy of that guess. My thanks also go to Mr. Tom Gaspar and Ribbon Technology Corporation for their support of the project. Finally, and most importantly, I would like to thank my parents and family for all their love and support through the years.

TABLE OF CONTENTS

Section	Page
I. Introduction	A-7
II. Method	A-9
III. Results	A-19
IV. Discussion	A-22
V. Conclusion	A-24
VI. Figures	A-25
VII. Appendix I	A-56
VIII. Appendix II	A-58
IX. Appendix III	A-62
X. References	A-64

I. Introduction

The promise of improvements in the magnetic, mechanical, and corrosion properties of a number of alloys has led to great interest in rapid solidification processes such as the melt overflow method. Previous studies [2,3] have shown that rapid cooling rates, on the order of 10^5 to 10^6 K/s, are necessary for the formation of the amorphous or microcrystalline phases which produce the property improvements. In general, the rapid solidification processes used to produce these high cooling rates can be characterized as ones in which a large, cold substrate extracts heat from a thin section of melt. The melt overflow process developed by the Ribbon Technology Corporation is one such method.

In the melt overflow process, a ribbon of metal is formed by the contact of molten metal in a specially shaped hearth with a rotating cylindrical chill block (Figure 1). Heat is extracted from the molten metal by the chill block, and the metal solidifies into a thin ribbon, which is carried off by the momentum imparted to it by the rotating chill block. Due to the high cooling rates involved in the process, amorphous or microcrystalline phases may appear in the microstructure of the ribbon. This microstructure in turn affects the characteristic properties of the solidified metal.

The experimental configuration studied uses a water cooled chill block 25.4 cm in diameter, made of copper, bronze, or steel. The metal is first melted in a copper hearth, which consists of a cylindrical bowl 10 cm in diameter and 4 cm deep, machined into a solid block of copper. An angled pouring lip is also machined into the block. The test setup being investigated utilizes a 75 kW plasma arc torch to melt a titanium alloy. The torch is centered over the hearth, but may also be made to traverse across the top surface of the melt (Figure 2). Once the metal is melted, the hearth is tipped toward the wheel, allowing the metal to come into contact with the rotating chill block, where it then solidifies into a thin, continuous ribbon. The top surface of the melt is exposed to the local environment throughout the process.

A number of factors influence the formation of the ribbon. These can be divided into two main groups. The first group is the material properties, such

as density, viscosity, and surface tension, which are inherent properties of the material being cast. The second group is the processing parameters, such as the speed of rotation of the chill block, and the intensity and location of the torch used to heat the metal, the hearth material, wheel material, coolant application, etc. These factors are dependent on the experimental prototype which is being studied. It is the purpose of this study to investigate how these factors, individually and in combinations, affect the solidification process. In particular, one primary goal is to predict the thickness of the solidified ribbon. The thickness of the ribbon affects how the ribbon will solidify, which determines the microstructure.

The approach used was to construct a finite element model which simulates the fluid and heat flow in the solidification process. Process dynamics, which determine ribbon thickness and freezing rate, were incorporated into this model through the material properties, geometry and boundary conditions. The thickness of the ribbon was solved for in the simulation, and by examining the velocity and temperature profiles calculated in the model, the cooling rate in the ribbon could be determined and the resulting microstructure estimated. The model is two-dimensional and can be thought of as a thin slice passing through the centerline of the hearth and chill block. With the model, the effects of a number of variables can be studied more quickly and easily than is possible with an experimental prototype of the process. It is possible to change a parameter, such as the speed of rotation of the chill wheel, merely by changing one or two numbers in the input file and rerunning the model. Additionally, parameters that would be difficult or impossible to change in an experiment, such as material viscosity or surface tension, can be investigated with the model. In this way, the influence of single parameters or combinations of parameters can be studied.

Once the temperature profile in the solidifying ribbon was known, it was possible to estimate the microstructure of the ribbon. For a typical alloy, variation in the values of G , the imposed temperature gradient, and V , the growth rate of the cells or dendrites, affects the resulting microstructure in the material. The ratio of G to V determines the morphology of the material. Low G/V values indicate plane front or cellular growth, while higher values indicate dendritic growth. The product of G and V , which is equal to the

cooling rate T for one dimensional heat flow, determines the spacing of the cells or dendrites. For low values of GV , coarse cells or dendrites would be expected, while high values indicate fine spacings (Figure 3) [4]. Studies have indicated that cooling rates in the range of 10^5 to 10^6 K/s are necessary to produce the desired properties in the rapidly solidified metal. If these rates cannot be achieved, undesirable growth morphologies or spacings may appear in the material and limit its applications.

II. Method

The commercial finite element code FIDAP, developed and marketed by Fluid Dynamics International of Evanston, Illinois, was used for the model. FIDAP is designed to analyze viscous incompressible fluid flows, both isothermal and temperature dependent [5]. Some of the specific features of this code will be discussed later. The analysis was run primarily on a Sun 3/280 computer with some additional work done on a Silicon graphics Iris 3020 workstation.

The solution process consisted of four major sections (Figure 4). First, a velocity solution was obtained, assuming constant temperature and a fixed ribbon thickness. This solution was then used as an initial estimate for the next solution, where the temperatures were assumed constant, but the ribbon thickness was computed. Next, the first solution was used as an initial estimate for an advection-diffusion solution to a thermal problem to obtain an estimate for the temperature field. Finally, the advection-diffusion solution and the free surface solution were used as a starting point for the fully coupled velocity and temperature solutions. Laminar flow of the fluid was assumed throughout the solution process. Each section of the solution procedure is described in detail below.

This step-by-step approach to the solution was used to ensure that the model was properly constructed and to diminish the effect of any nonlinearities in the problem on the solution process. It is important to note that none of the four sub-problems in the solution process is particularly easy to solve. The mesh geometry and density, the material properties, the velocity and temperature boundary conditions, and the solution procedure used all

have major impacts on these problems and an error in any of these areas can result in either nonconvergence of the solution or an inaccurate solution. By taking a step-by-step approach to the solution, these errors can be dealt with as they arise and confidence can be taken that the final answer obtained is indeed correct.

It is also important to note that the final solution to the coupled velocity and temperature problem includes in it all the important features of the melt overflow process. Since the free and fixed velocity solutions and the advection-diffusion solution are used as input to the coupled problem, all the process features included in these solutions are carried over to the coupled solution. Thus, a true representation of the physics of the melt overflow process appears in the solution to the coupled velocity and temperature problem.

The first step in the construction of the model was the formation of the finite element mesh. Because we were primarily interested in the solidification process, only the melt itself was included in the model. The effects of the torch, hearth, and chill wheel were taken into account through the boundary conditions for the model. To allow a greater element density in the ribbon area and to reduce computational time, only half of the melt in the hearth was included in the model. Symmetry was assumed along the hearth centerline. This is not strictly correct, but the approximation should have negligible effect on the modeling of the ribbon formation, because the asymmetry appears far from the symmetry plane.

The geometry of the finite element mesh was set up to resemble that of the experimental melt overflow process being used by Ribtec. The model was constructed for a hearth tip angle of 5 degrees from horizontal. The thickness of the ribbon was initially estimated as 0.25 cm. The rest of the dimensions of the model are shown in Figure 5. The mesh was generated by first specifying 16 major keypoints in integer and geometric space. The keypoints were connected with lines or curves and surfaces were created by specifying their corners.

The elements used for the melt were four noded linear isoparametric quadrilateral elements (Figure 6). The pressure degrees of freedom were constant within each element, and not continuous across element boundaries. A discretized pressure variable was used, adding an additional degree of freedom to the problem. While it is sometimes possible to use a penalty method to eliminate the pressure variables, it was not advisable to do so for the free surface velocity solution due to nonlinearities which can appear in the model [6]. For consistency, the mixed formulation, retaining pressure degrees of freedom, was used throughout the solution process.

In addition to the quadrilateral elements, two noded boundary elements were created on the top of the melt surface, on the melt-chill wheel interface surface, and on the melt-hearth interface surface (Figure 7). Boundary elements have a local normal and tangential coordinate system which facilitate their use in imposing convective and radiative heat flux boundary conditions and in defining free surface boundaries. In order to use the velocity solution as input later to the temperature problem, two sets of boundary elements were defined along the same surface to allow for the application of boundary conditions in the temperature solution, as well as the velocity solution. An example of this is along the top surface of the melt where there were velocity slip elements and, in the temperature solution, radiation boundary elements. Doubly defined boundary elements also existed on the melt-chill wheel interface surface and the melt-hearth interface surface. For the velocity solution only, the two sets of boundary elements were identically defined. The full mesh consisted of 1808 nodes and 2167 elements (Figure 8).

FIDAP allows for the use of both constant and temperature dependent material property values in the analysis. The temperature dependence of viscosity, specific heat, thermal conductivity, surface tension, and the thermal heat transfer coefficient may all be described by a series of points defining a temperature-material property curve. Since the fluid being modelled was assumed to be incompressible, the fluid density must be constant. The material property values used in the model were those of pure titanium and are listed in Appendix I. All values used were in the cgs system.

The surface tension value played a major role in the solution of the free surface problem. In addition to the value of the surface tension, the solution procedure required that values of two angles be provided, corresponding to the contact angles that the tangent to the surface made with the global x-axis at the ends of the surface (Figure 9). These angles were necessary to provide continuity with the rest of the mesh at the fixed end points of the free surface.

A temperature dependent curve for viscosity was included in the model for the temperature solutions. This curve used the value of 0.04 g/cm-s [7] for the viscosity of the metal above the solidification temperature and 1×10^{22} g/cm-s for the solidified metal. The latent heat of fusion for the metal was included either as a temperature dependent specific heat curve (Figure 10), or through a temperature dependent enthalpy curve, using a technique developed by Lemmon [8] and implemented by Dantzig [9] (Figure 11). In the former case the area under the spike in the curve was equivalent to the latent heat of fusion, and in the latter case the latent heat is given by the enthalpy difference at the freezing point.

The solution process began with a steady-state, isothermal solution to the velocity problem, using a mesh for an assumed fixed ribbon thickness. At this point the energy equation was not included and only the momentum equations, without the buoyancy terms, were solved. The governing equations for this problem are;

$$\begin{aligned} \rho \mathbf{U} \cdot \nabla \mathbf{U} &= -\nabla p + \mu \nabla^2 \mathbf{U} \\ \nabla \cdot \mathbf{U} &= 0 \end{aligned} \quad (1)$$

where ρ is density, \mathbf{U} is velocity, p is pressure, and μ is viscosity. A steady-state analysis was performed using Stokes flow as the initial iterate for the solution. In Stokes flow, the convective term on the left-hand side of Eq. (1) is ignored. This provided a reasonable initial estimate, allowing convergence in the solution procedure used for the full nonlinear problem [10].

Several solution techniques, such as successive substitution, Newton-Raphson, and quasi-Newton, were possible for these problems. In general,

successive substitution had the best convergence radius, but took the largest number of iterations to converge. Conversely, the Newton-type methods required fewer iterations, but had smaller radii of convergence. It was possible to speed up convergence by starting the solution with several iterations of successive substitution, then switching to one of the Newton-type methods. Typically, three steps of successive substitution were used followed by ten steps of quasi-Newton to obtain solutions. For all the problems, convergence was declared when the relative changes in the solution iterates changed by less than 0.1%, and the residuals were also less than 0.1% of their initial values.

The boundary conditions imposed on the model for the fixed ribbon velocity solution are shown in Figure 12. Along the bottom edge of the mesh, where the melt is in contact with the copper hearth, both the normal and tangential components of velocity were set to zero. Along the top surface of the melt, the normal component of velocity was set to zero. The surface representing the interface between the ribbon and the chill block has a normal velocity of zero, and tangential velocity equal to the tangential speed of the rotating chill. The boundary conditions on the remaining surfaces were left free, corresponding to no shear stress. A typical input file for the fixed ribbon velocity problem appears in Appendix II.

Solutions were obtained corresponding to a number of experimental conditions. The tangential velocity of the chill wheel was varied between 1.0 and 10.0 m/s to simulate different casting rates. The viscosity was also varied to study its affect on the solution. Several mesh densities were also tried to study the effect on convergence.

Once these solutions were obtained, they were used as initial guesses to obtain the velocity solution which estimated the thickness of the solidified ribbon. FIDAP is able to solve fluid flow problems which include free or moving fluid boundaries which satisfy the following criteria: the models must be two dimensional and the moving surface cannot undergo major changes in shape or position compared to the initial mesh [11]. For this model, neither of these limitations posed a major problem. The model was already being approached as a two dimensional problem, and by using some care in the

choice of the initial mesh for the free surface problem convergence problems associated with major shape and position changes were avoided.

The top surface of the melt in the vicinity of the ribbon was designated as a free surface in this problem. The nodes on this surface were allowed to move with respect to a series of specified reference points, and their final positions were calculated by the program. This was done by introducing an additional degree of freedom for the position of the nodes on the free surface. If these nodes were allowed to move indiscriminately, the element mesh could become severely distorted. To prevent this, the motion of the free nodes was constrained to remain along a set of pre-designated line, referred to as spines, in such a way that the initial distance ratio between the moving nodes on each spine is always maintained (Figure 13). The reader is referred to reference [12] for further details.

Because the nodes were free to move along the spine in the solution procedure, it was important to start with a set of spines which were as nearly perpendicular to the final streamlines as possible, within the general restrictions of the problem geometry. If this were not done, movement of the nodes along the spines could cause elements to become severely distorted and result in a solution which failed to converge. Keeping the spines reasonably parallel reduced or eliminated this problem in most instances. Increasing, or in some cases reducing, mesh density in the region of the spines could also reduce convergence problems associated with element distortion.

In order to better understand this free surface problem, a smaller model of the ribbon region was constructed (Figure 14). This model had the same basic dimensions as the larger version, but contained only the ribbon itself and a portion of the fluid leading up to it. Since the free surface problem was difficult to solve because of the added degrees of freedom at the free nodes, and the small radius of convergence of the Newton-type methods used to solve it, an initial mesh which was close to the ultimate solution was necessary. By constructing the smaller model of the ribbon region, it was possible to make the necessary adjustments to the mesh and rerun the model in less time than would have been required to solve the larger model from the outset. It was often necessary to make several mesh adjustments before a converged solution

was obtained. Changes in material properties and processing parameters also necessitated a change in the initial mesh. Once experience with the solution of free surface problems was gained, the results from the smaller model were incorporated in the complete model of the process.

The geometry of the complete free surface model was the same as that used for the fixed ribbon velocity solution. Four noded quadrilateral elements were again used for the melt itself with two noded boundary elements on the outside surfaces. The material properties were the same as those for the fixed ribbon velocity problem, with the addition of surface tension, which plays an important role in the free surface solution. The boundary conditions were similar to those in the fixed ribbon problem, with one important exception. For the free surface solution, the zero normal velocity boundary condition on the top surface of the melt was removed to allow this surface to move (Figure 15). The final solution will automatically satisfy this condition. A typical input file for the free surface velocity solution appears in Appendix II.

The isothermal fixed ribbon and free surface velocity solutions were next used to obtain temperature solutions for the problem. First, the fixed ribbon solution was used to solve the associated advection-diffusion problem. In this case, only the energy equation was solved, the velocity solution being in from a restart file, and assumed to be unchanged. The governing equation for this problem is;

$$\rho C_p \mathbf{U} \cdot \nabla T = k \nabla^2 T \quad (2)$$

where ρ is density, C_p is specific heat, \mathbf{U} is velocity, T is temperature, and k is thermal conductivity.

The mesh used for the temperature solution was the same one used for the velocity solution, and there were again a number of boundary conditions to be considered (Figure 16). At the surfaces where the melt was in contact with the hearth, convective heat transfer takes place. Convective boundary elements were specified on these surfaces. This type of element requires that a value for the heat transfer coefficient and T_∞ be provided. The heat transfer

coefficient used for the melt-hearth interface was the ratio of thermal conductivity for the copper hearth, k_{Cu} , to the average thickness of the hearth, Δx . The value for this model was 0.1 cal/cm-s-C. T_{∞} was 25 C, corresponding to cooling water.

At the surface where the ribbon was in contact with the chill block, convective heat transfer was again considered the most important heat transfer mechanism present. Convective boundary elements were again specified. The heat transfer mechanism in this area is not well understood and previous studies of heat transfer in rapidly solidified metal ribbons have assumed that the metal was in contact with the chill wheel for some period of time, with the convection between these two surfaces dominating the heat flow [13]. However, studies in continuous castings have shown that as the metal solidifies it shrinks away from the surrounding mold and an air gap forms between the metal and the mold. The heat transfer coefficient in these problems was modelled as a combination of conduction and radiation across the air gap [14]. This study initially assumed that a process similar to that in continuous casting occurs in the melt overflow process, and the heat transfer coefficient used for the ribbon-chill block contact surface was similar to values used in continuous casting simulations (0.05 cal/cm²-s-C)

Along the top surface of the melt, radiative heat transfer dominates. Here, radiative boundary elements were specified. This type of element requires that the emissivity, the Stefan-Boltzmann constant, and T_{∞} be provided. A value of 0.2 was used for the emissivity of molten titanium [15], the Stefan-Boltzmann constant, in the appropriate units, was 5.67×10^{-12} cal/cm² - s-K⁴ and T_{∞} was 25 C.

Finally, a distributed heat flux was applied to top of the melt to simulate the plasma arc torch used to heat the titanium. In the absence of accurate data describing the torch being used in the experimental setup, two approaches were taken. In one approach, a ramped heat flux was used to simulate the torch (Figure 17). The heat flux extended across the top of the melt to the same diameter as the bowl of the hearth. The area under the ramped curve was equated to half of the 75 kW power of the torch, since the model was assumed to be symmetric about the hearth centerline, and the heat flux to be applied at

each node in the affected area was calculated. In the second approach, a Gaussian distribution was assumed for the torch and the same affected area was used (Figure 18). The area was again equated to half of the torch power and the heat flux at each node was calculated. Since it was possible to move the torch across the top of the melt, different torch locations were investigated.

The thermal boundary condition on the two remaining surfaces, the top surface of the ribbon and the edge of the melt at the righthand side of the model, were left free. The condition that was then applied by FIDAP was that $q=0$ on these surfaces. Note that the ribbon actually continues past the ends of the mesh and the righthand side of the model was actually the centerline of the bowl of the hearth.

In addition to the thermal boundary conditions, velocity boundary conditions were required on most of the same surfaces. These were the boundary conditions which were doubly defined in the velocity solution. On the top of the melt, the ribbon-chill wheel interface, and the melt-hearth interface, boundary slip elements were defined to keep the velocity vectors in the local normal-tangent coordinate system.

Solutions of the thermal problem were obtained for a number of different combinations of variables. The main variables were the speed of rotation of the chill block, the heat transfer coefficient at the ribbon-chill wheel interface, the method of incorporating latent heat of fusion into the problem, and the intensity and location of the heat flux for the torch.

The advection-diffusion solution was close enough to the final solution that the velocity and temperature solutions could be solved in a coupled analysis using the quasi-Newton procedure [16]. The isothermal, free surface, velocity solution was then the initial guess for the velocity solution, and the advection-diffusion solution provided the initial guess for the temperature solution. The complete momentum and energy equations were then solved together. The buoyancy term remained discarded from the momentum equations. The governing equations for the coupled velocity and temperature problem are;

$$\begin{aligned}
\rho \tilde{U} \cdot \nabla \tilde{U} &= -\nabla p + \mu \nabla^2 \tilde{U} \\
\rho C_p \tilde{U} \cdot \nabla T &= k \nabla^2 T \\
\nabla \cdot \tilde{U} &= 0
\end{aligned}
\tag{3}$$

A typical input file for both the advection-diffusion and the coupled problems appears in Appendix III.

For free surface problems, Newton-type solution methods are generally used since they eliminate the need to interpolate the velocity degrees of freedom at the free nodes to their new locations at every iteration [17]. This necessitated that a "good" initial guess for the velocity solution and the initial mesh be available because of the smaller radius of convergence of these solution techniques. The velocity solution for the fixed ribbon problem was thus used as this initial guess.

It was often possible to obtain a converged solution for a particular set of conditions by starting with a converged solution for a different set of conditions. For example, it was possible to obtain a velocity solution for low viscosity values, 0.04 g/cm-s, by first obtaining a velocity solution at a higher viscosity value, such as 1.00 g/cm-s, and using that solution as the initial guess for the low viscosity solution. This approach was usually successful over a wide range of values and was often the fastest way to obtain a set of converged solutions. It was of particular use in the solution of the free surface problem, which had an inherently small radius of convergence. It was generally easier to solve the free surface problem by starting with an initial mesh in the ribbon region which was smaller than the final free surface mesh in this region. Whether this is true of free surface problems in general is unknown.

For the advection-diffusion solution and the coupled solution it was possible to use either successive substitution or the Newton based solution techniques. The same time versus convergence tradeoffs discussed earlier were applicable, and typically the quasi-Newton method was used.

III. Results

The values of the speed of rotation of the chill wheel, and the viscosity of the melt were varied to determine how they affected the velocity solution. The solution consists of the magnitude and direction of the velocity at each node, and the pressure in each element in the mesh. From this information the velocity streamlines can be calculated.

The solutions to the fixed ribbon velocity problems studied exhibit some common characteristics (Figures 19-23). The magnitude of the vectors in the hearth portion of the melt is low and the vectors are directed toward the ribbon, as would be expected since the driving force in the velocity problem is the momentum imparted to the melt by the rotating chill wheel, which directs the flow away from the hearth. The velocity of the melt increases along the pouring lip, approaching the chill wheel. In the ribbon region, a momentum boundary layer forms, originating at the wheel side of the ribbon and growing outward.

For a constant wheel velocity value, changes in viscosity resulted in changes in the velocity profile of the region in the immediate vicinity of the melt-chill block interface. For low values of viscosity (< 0.2 g/cm-s) a small recirculation zone was found in the area of the initial point of contact of the melt with the chill wheel (Figure 19). Similar recirculation zones have been seen in analyses of planar flow casting in aluminum [18]. The viscosity also had an effect on the thickness of the momentum boundary layer, with the thickness of this layer being smaller at low viscosities compared to high viscosities (Figure 20).

Changes in the velocity of the rotating chill block also has an effect on the velocity profile of the fixed ribbon. Changes in velocity effect the vector profile in much the same way changes in viscosity effect it. For low viscosity values, high velocities make the recirculation zone more pronounced than lower velocities (Figure 21). The thickness of the momentum boundary layer is also thicker at higher velocities than at lower velocities (Figure 22).

The depth of the melt on the pouring lip also affected the velocity profile in the melt. The mesh was constructed by assuming that the top surface of the melt was horizontal, and at the same height as the end point of the pouring lip (Figure 5). Decreasing the depth of the melt on the pouring lip had little effect on the size of the recirculation zone (Figure 23).

Once a satisfactory model for the fixed ribbon velocity solution was obtained, the free surface velocity solution was attempted. Once again, the velocity of the chill wheel and the viscosity of the melt were varied. These two values, along with the surface tension value, played the major roles in determining the thickness of the ribbon. Now, the viscosity of the melt had a direct influence on the thickness of the resulting ribbon. For a constant velocity, a high value for viscosity (100 g/cm-s) resulted in a ribbon thickness on the order of 200 microns. As viscosity was reduced, the thickness of the ribbon increased to about 5000 microns (Figure 24).

The chill wheel velocity also affected the thickness of the ribbon in much the same manner as viscosity. For a constant viscosity, a high velocity value created a thin ribbon and decreasing the velocity increased the ribbon thickness. The similarity in the effects of viscosity and velocity makes sense when one realizes that when the governing equations are non-dimensionalized, the parameter which appears is capillary number, $Ca = \mu U / \sigma$. Increasing the velocity or viscosity increased the capillary number and resulted in a thinner ribbon. Similarly, decreasing the surface tension increased the capillary number and also resulted in a thinner ribbon. The effect of capillary number on ribbon thickness is shown in Figure 25. Increasing velocity or viscosity increased the capillary number and resulted in a thinner ribbon. Similarly, decreasing surface tension increased the capillary number and also resulted in a thinner ribbon.

The depth of the melt leading into the ribbon also had an effect on the thickness of the ribbon. It was again assumed that the top of the melt would be a horizontal line at the same height as the end point of the pouring lip. If the depth was increased, the thickness of the ribbon increasing correspondingly. An increase of 0.1 cm in depth lead to an increase of about 200 microns in the ribbon thickness (Figure 26).

The advection-diffusion temperature solution was first solved using the fixed ribbon velocity solution. Typical temperature profiles for this type of problem are shown in Figures 27-31. The temperature was very high directly beneath the torch and falls off quickly away from the torch. The effect of cooling on both sides of the pouring lip, radiation on the top surface and convection on the bottom, can be seen in the temperature profiles in this region. The influence of the chill wheel can be seen in the ribbon region, with the isotherms moving outward from the chill wheel side of the ribbon.

The intensity of the torch influenced the magnitude of the temperature profiles in the melt, but did not change the shape of the profiles significantly. Figure 27 shows the profiles for torch values of 75 kW and 50 kW for a gaussian heat flux. Using a ramped heat flux in place of the gaussian flux changes the temperature profile directly beneath the torch, but had little effect on the temperature profiles in the pouring lip and ribbon (Figure 28).

The value of the convective heat transfer coefficient used on the chill wheel side of the ribbon played a major role in the solidification characteristics of the ribbon, but had little influence on the thickness. This was also a surprising result. The initial value, $0.05 \text{ cal/cm}^2\text{-s-C}$, used was consistent with values used for continuous casting models, discussed earlier. However this value proved to be too low for this model, since temperature isotherms in the ribbon show that the ribbon would not have solidified before leaving the wheel (Figure 29). This is inconsistent with experimental observations. Increasing the value to 7.0 to $8.0 \text{ cal/cm}^2\text{-s-C}$, consistent with values found in other studies of rapid solidification processes [19], resulted in an isotherm for the solidus which originated close to the initial point of contact between the melt and the chill wheel, and ended on the top surface of the melt (Figure 30). This meant that the ribbon has solidified completely when using the higher value for h_{wheel} .

Based on the isotherms and the velocity of the chill wheel being used, the cooling rate for the ribbon could be estimated. First, two points on the ribbon surface were chosen and the temperatures at the points and the distance between them was obtained from the thermal solution. The change in time

between the points was calculated from the velocity and the distance. Finally the cooling rate was calculated from the temperature difference and the change in time. For a velocity of 5.0 m/s and h_{wheel} value of 7.0 cal/cm²-s-C the estimated cooling rate is 1.6×10^5 K/s. The temperature gradient, G , was estimated from the isotherms and the distance between them. For the same velocity and h_{wheel} values as before, a temperature gradient of 1×10^3 K/cm was estimated and a growth velocity, V , of 1.6×10^2 cm/s was calculated.

Using earlier solutions for the velocity problems and the advection-diffusion problem as input, the fully coupled velocity and temperature solution and free surface problem was solved. The temperature profiles from these solutions were essentially the same as those obtained in the advection-diffusion problems (Figure 31). The velocity solutions are also similar, with some changes in the pouring lip and ribbon region observed. Changes in the torch once again had the same effects in the coupled solutions as they had in the advection-diffusion solutions.

IV. Discussion

The fixed ribbon and free surface velocity solutions have shown that the viscosity of the melt and the velocity of the rotating chill wheel have the greatest influence on the velocity profile in the melt and the thickness of the resulting ribbon. Surface tension and the material depth on the pouring lip also influenced the velocity solutions.

In both the fixed ribbon and free surface solutions it was seen that viscosity and velocity influenced the formation of a recirculation zone in the melt just before the melt-chill wheel interface. The recirculation zone is not desirable because it allows cooling of the melt during recirculation and possible freeze-off of the metal before it reaches the chill wheel. This can best be avoided by keeping casting speeds low and maintaining a sufficient thickness of material on the pouring lip. While it is difficult to control the viscosity of the melt for any given metal, it is important to understand the influence of viscosity if other metals or alloys are to be cast. For similar casting speeds, metals with lower viscosities will experience more problems with recirculation and freeze-off.

Viscosity and velocity also played major roles in determining ribbon thickness. The results indicate that the thickness of the ribbon is dependent on the capillary number of the fluid and is determined by the shape of the meniscus before the ribbon solidifies. Results from the model agree well with early experimental results from the melt overflow process. This also indicates that the only practical way to change ribbon thickness is to change the velocity of the chill wheel, since both viscosity and surface tension, the other factors that determine capillary number, are difficult to change for a given material.

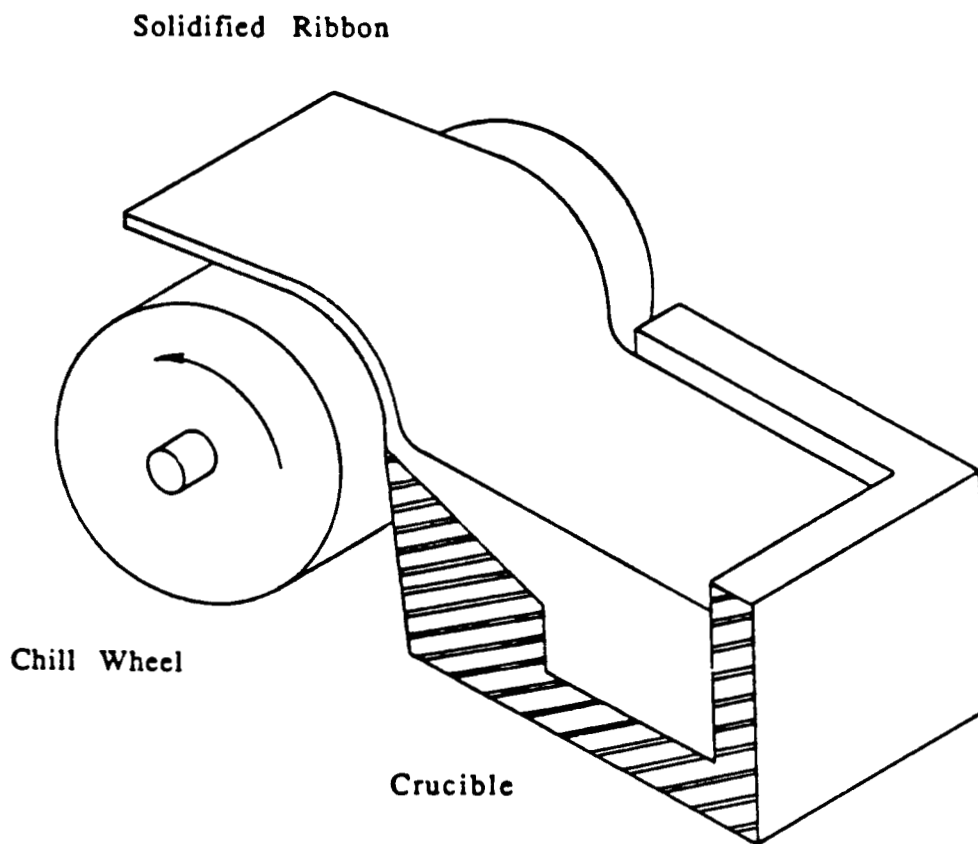
In the thermal results, the heat transfer between the melt and the chill wheel proved to be the main factor in the formation of the solidified ribbon. The conclusion reached, that h_{wheel} had to be between 7.0 and 8.0 cal/cm²-s-C for the ribbon to solidify, is in agreement with experimental rapid solidification studies, but disagrees with the initial assumption that the heat transfer mechanism occurring was similar to that of continuous casting. It is still unclear what sort of heat transfer mechanism takes place between the ribbon and the chill wheel and further study is needed to better understand this process.

The location and intensity of the torch also influenced the solidification of the ribbon. Raising the intensity or moving the torch closer to the ribbon raised the temperature of the melt in the ribbon and delayed solidification. The torch was modelled as a gaussian distribution with a power of 75 kW which was centered over the hearth. This type of distribution and power level may or may not be correct and as further experimental data on the torch becomes available, the torch heat flux should be modified accordingly.

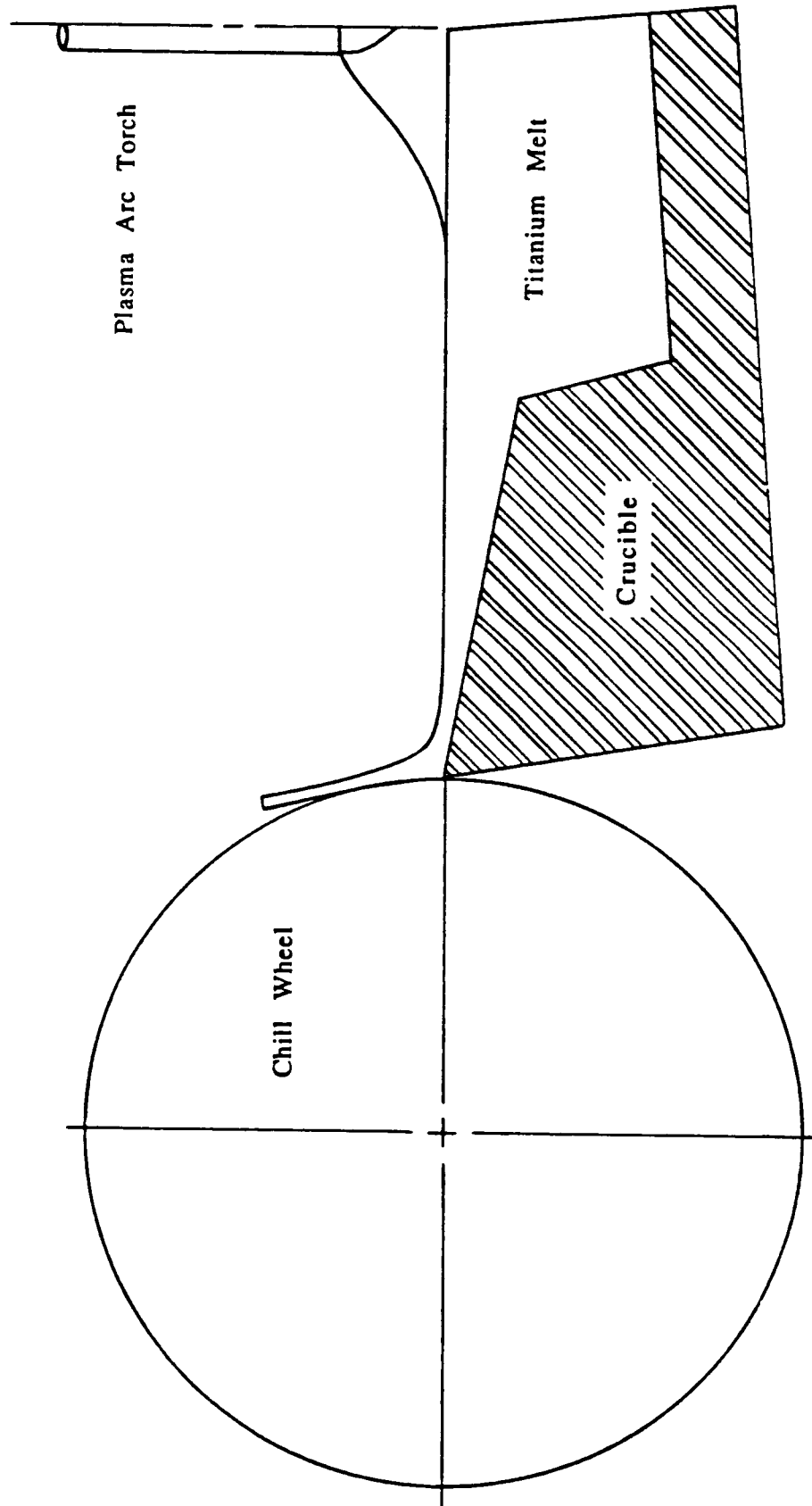
The cooling rate in the ribbon was calculated to be 1.6×10^5 K/s, which is also in agreement with other studies of rapid solidification processes. This cooling rate is within the region of 10^5 to 10^6 K/s necessary for the formation of amorphous or microcrystalline phases in the ribbon.

V. Conclusion

This study of the melt overflow rapid solidification process has shown that the process can be used to produce a thin, continuous ribbon with amorphous or microcrystalline phases in the microstructure. The capillary number, which relates the velocity of the chill wheel, and the viscosity and surface tension of the melt, appears to be the main factor in determining the thickness of the ribbon while the heat transfer coefficient between the ribbon and the chill wheel is the main factor in determining the location of the solidification front in the ribbon. Further work needs to be done to better understand the influence of the capillary number on ribbon thickness and to better understand the heat transfer mechanism between the ribbon and chill wheel.

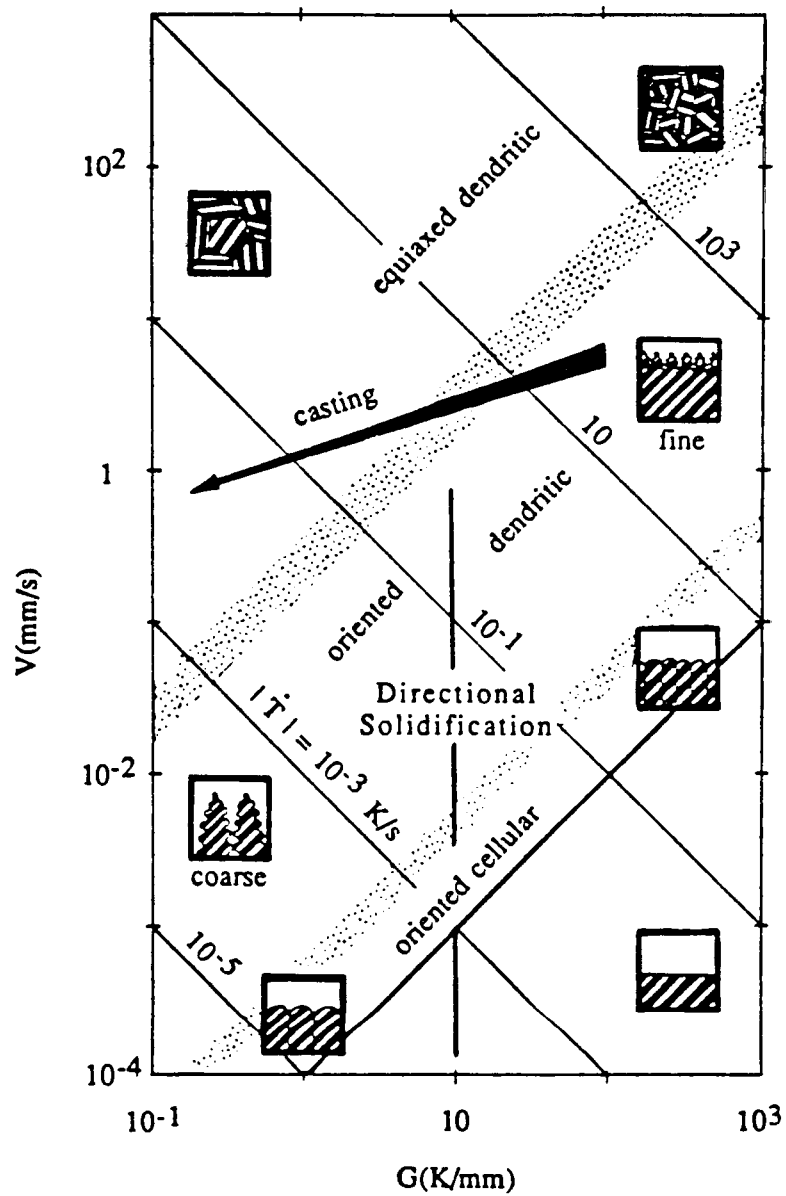


Melt Overflow Process
(Figure 1)

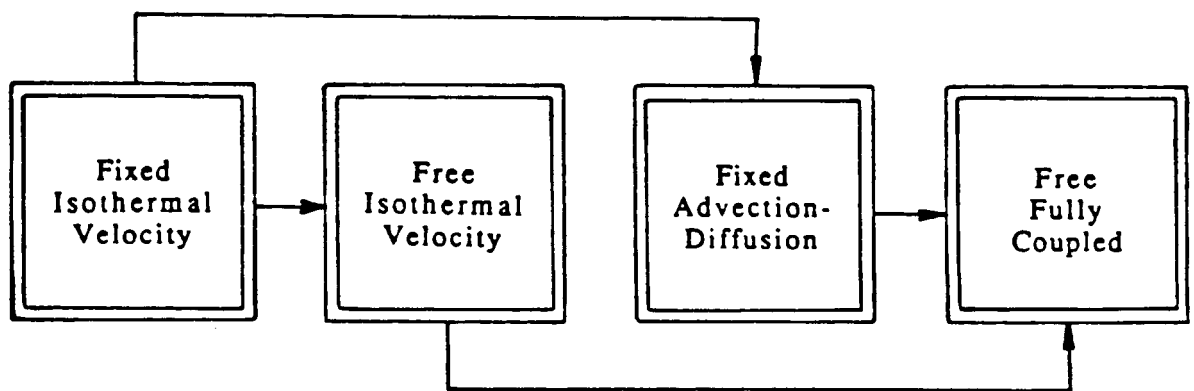


Experimental Setup

(Figure 2)

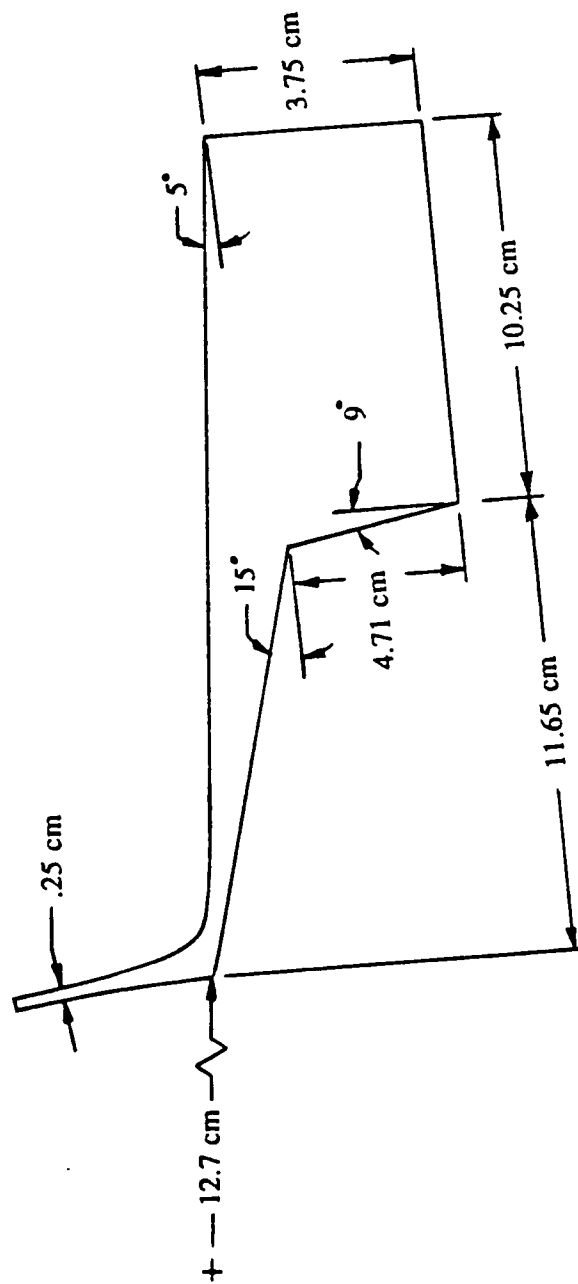


Influence of Temperature Gradient, G ,
and Growth Rate, V , on Microstructure
(Figure 3)



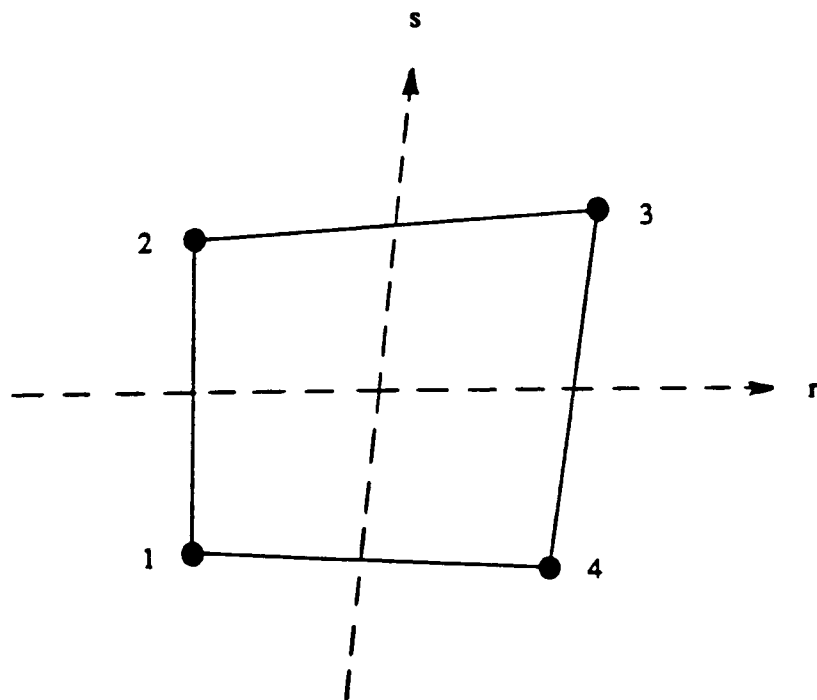
Solution Process

(Figure 4)



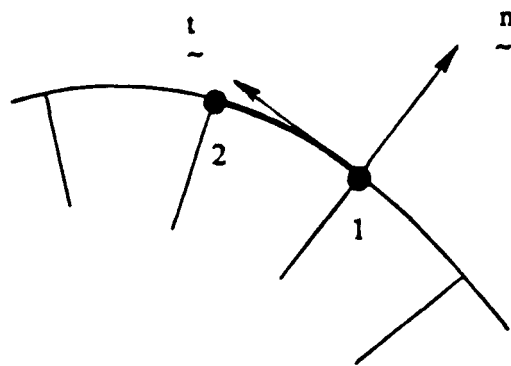
Model Dimensions

(Figure 5)

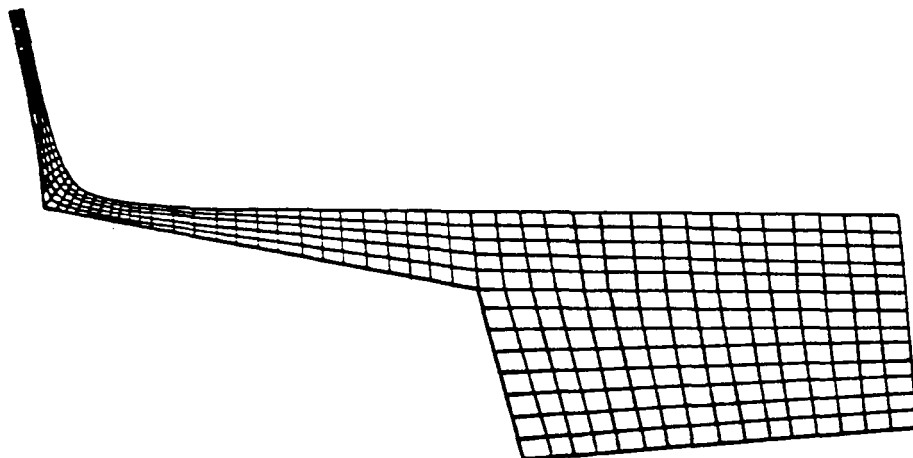


Four Noded Linear Isoparametric
Quadrilateral Elements

(Figure 6)

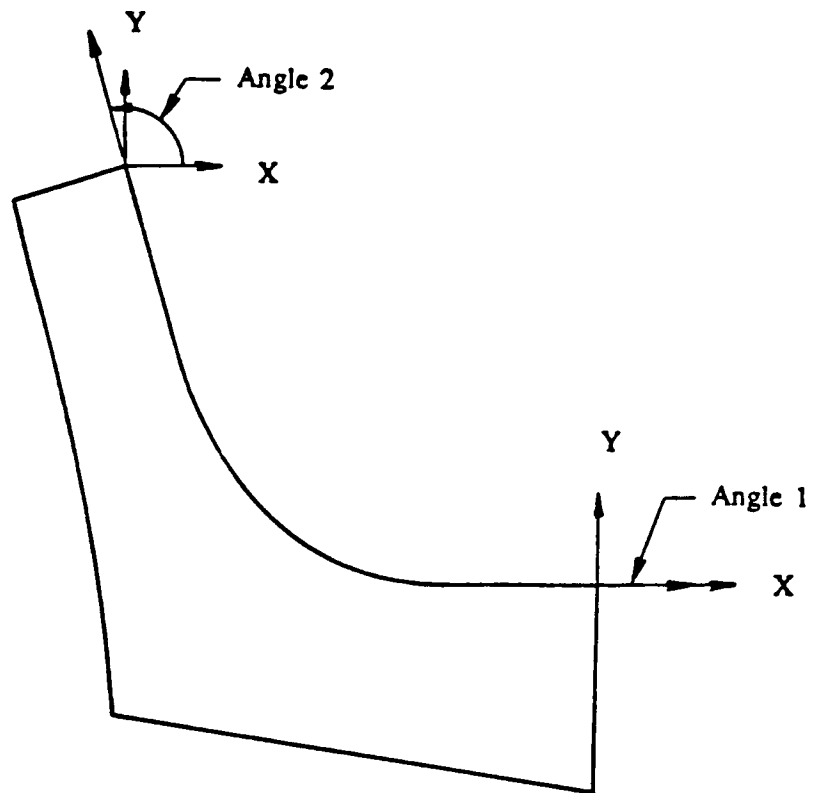


Two Noded Boundary Elements
(Figure 7)



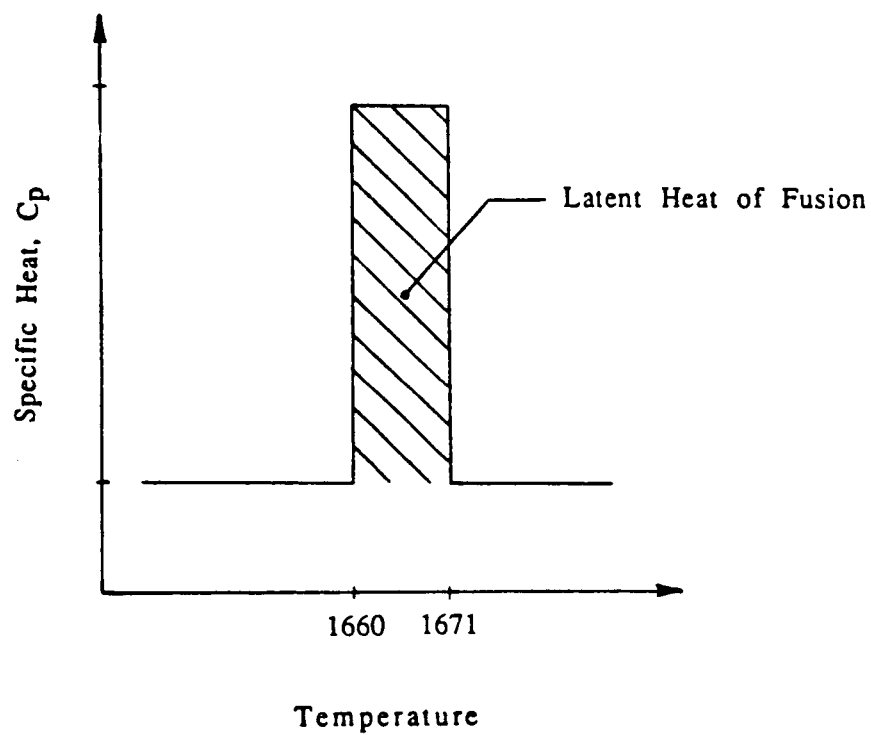
Finite Element Mesh

(Figure 8)



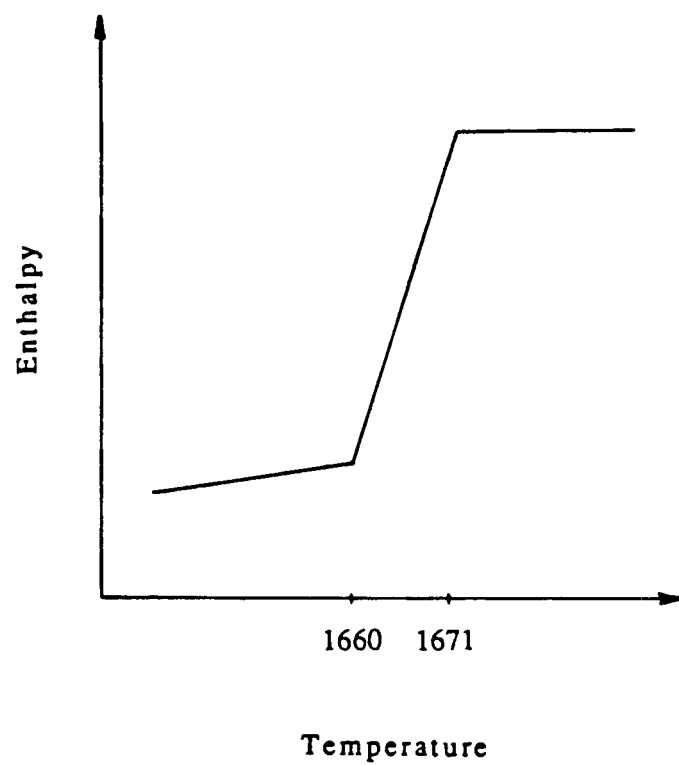
Surface Tension Angles

(Figure 9)

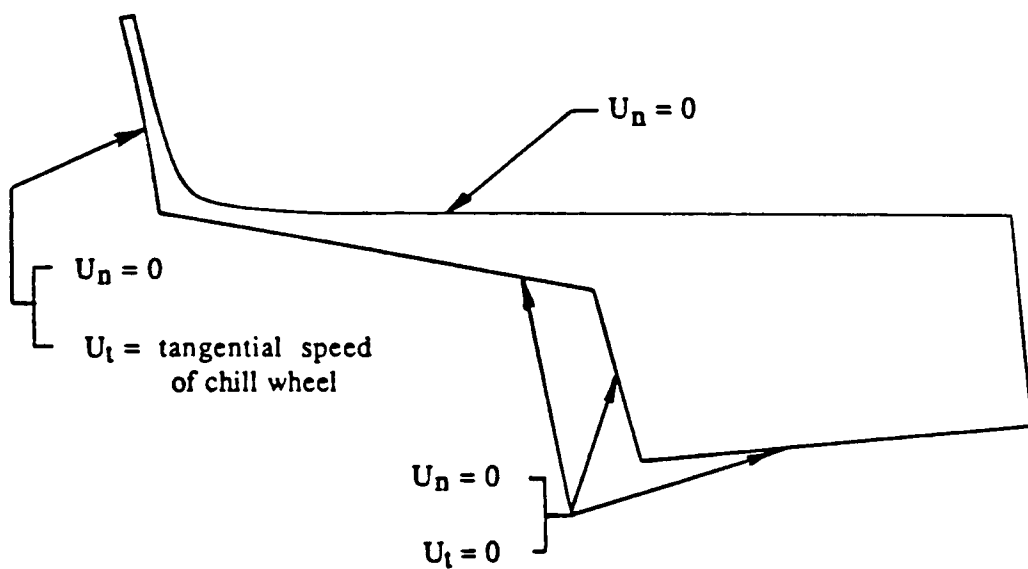


Latent Heat of Fusion - Specific Heat Method

(Figure 10)

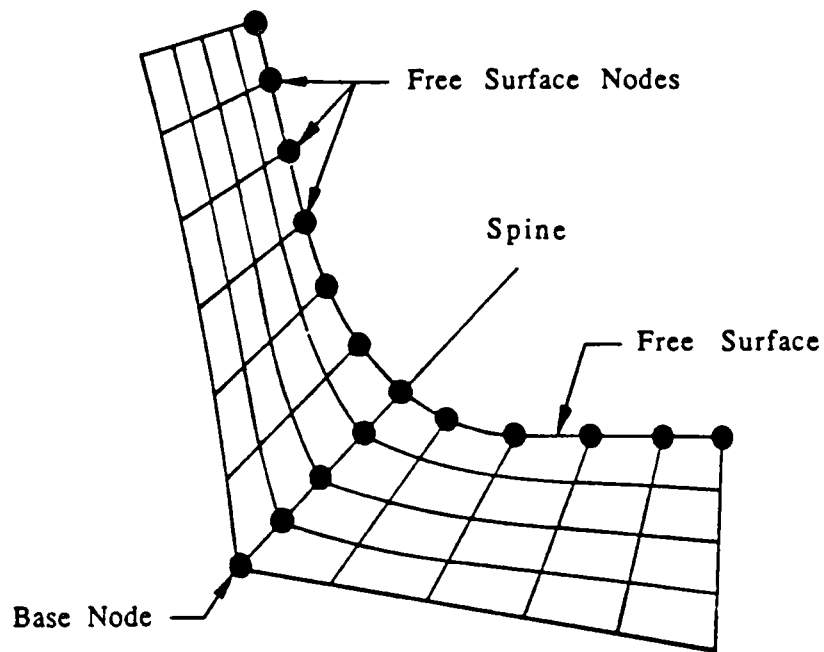


Latent Heat of Fusion - Enthalpy Method
(Figure 11)



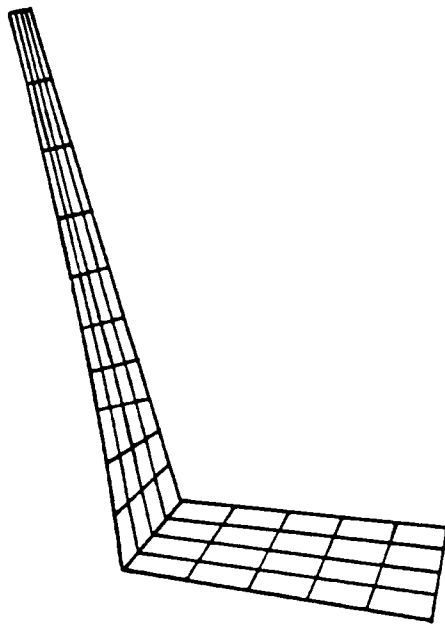
Velocity Boundary Conditions

(Figure 12)



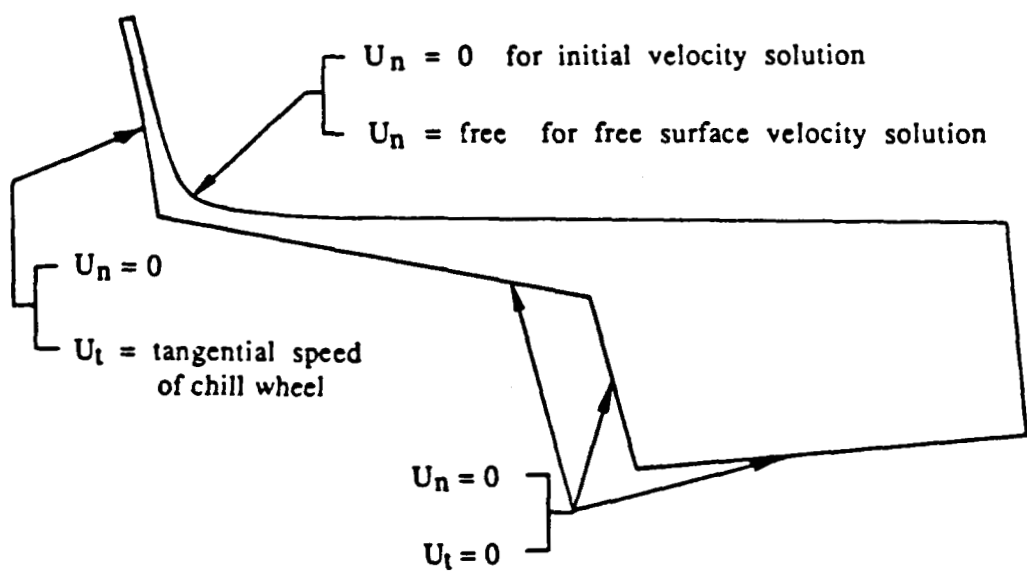
Free Surface Spines

(Figure 13)



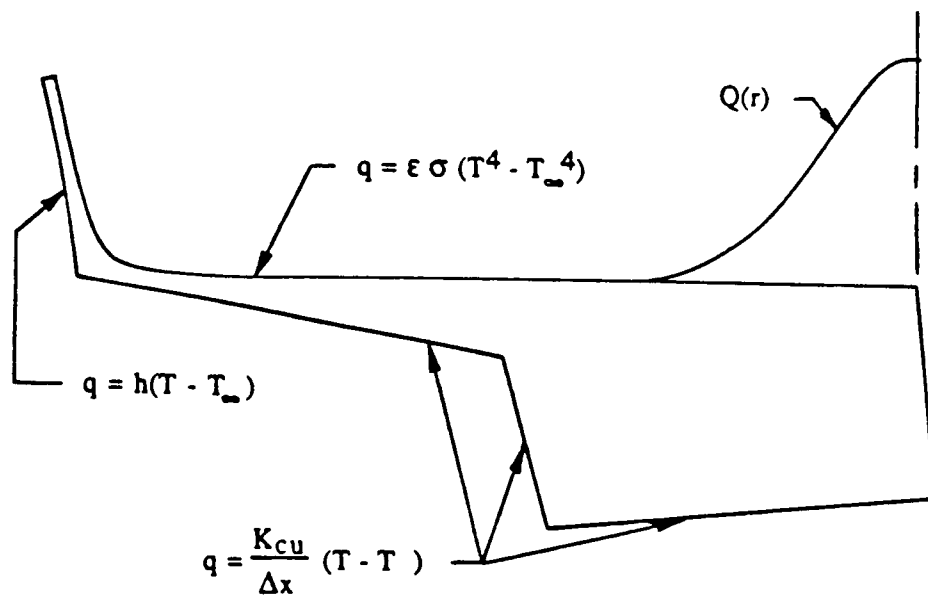
Small Model for Free Surface Problem

(Figure 14)



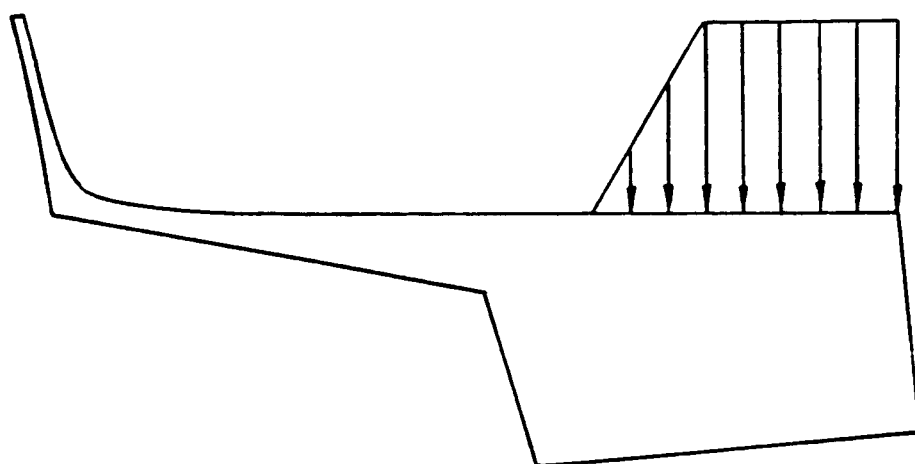
Free Surface Boundary Conditions

(Figure 15)

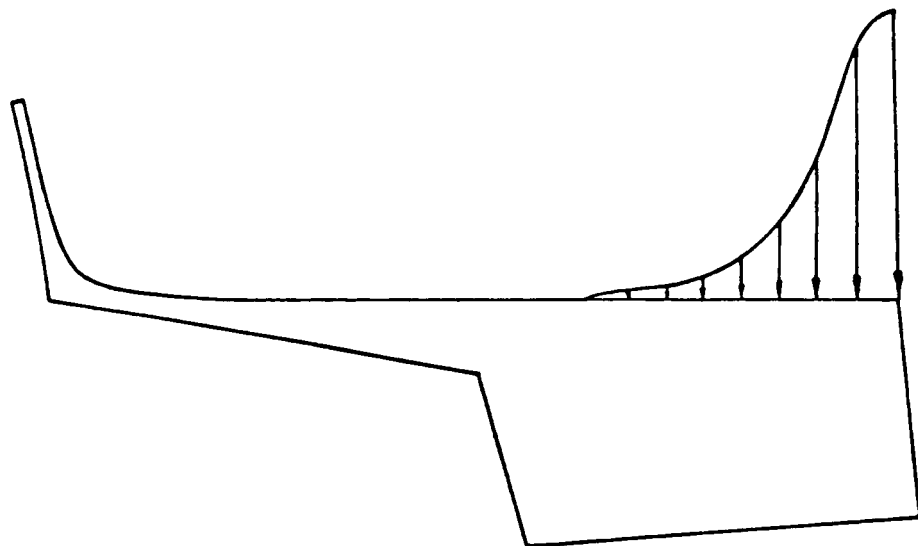


Temperature Boundary Conditions

(Figure 16)

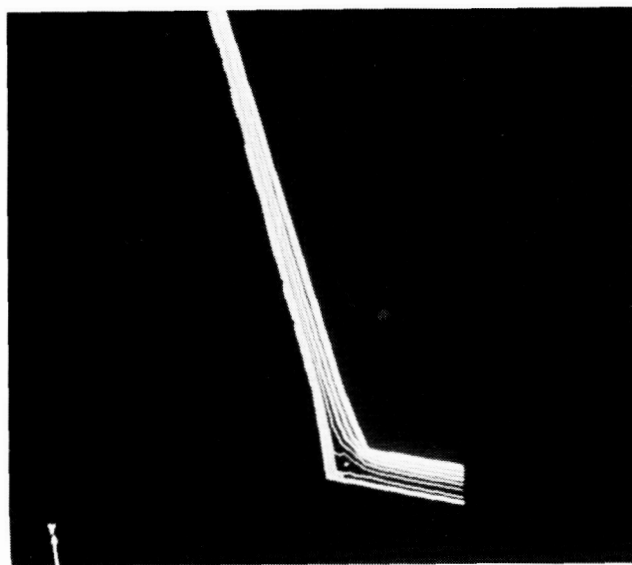


Ramped Heat Flux for Torch
(Figure 17)

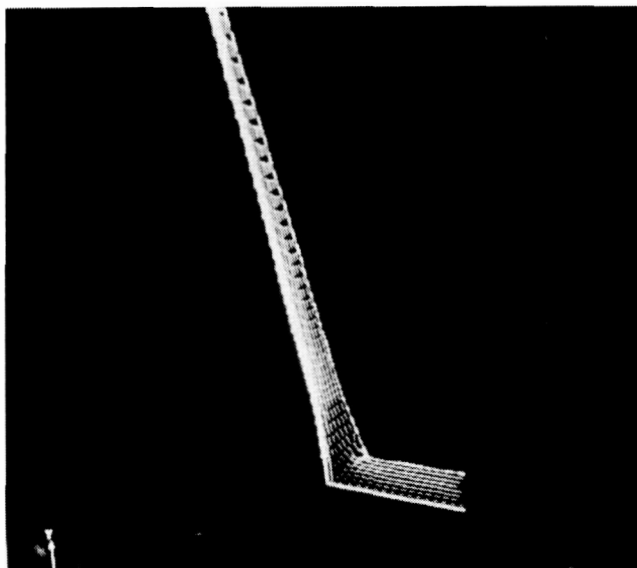


Gaussian Heat Flux for Torch
(Figure 18)

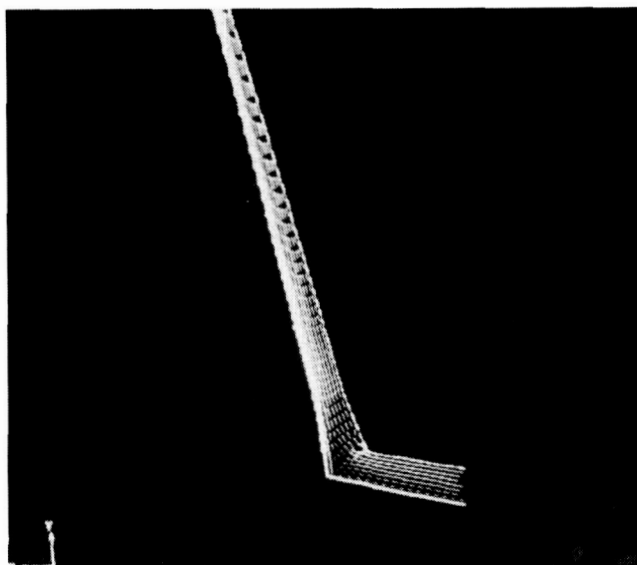
ORIGINAL PAGE
BLACK AND WHITE PHOTOGRAPH



Effect of Viscosity on the Formation
of the Recirculation Zone
(Figure 19)



low
viscosity

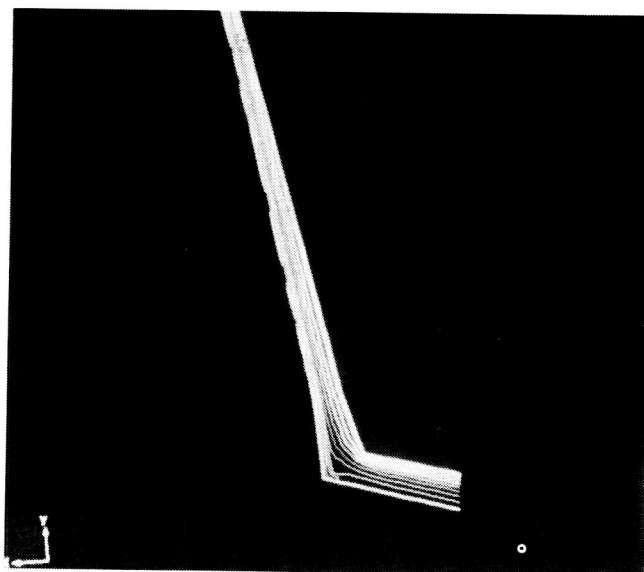


high
viscosity

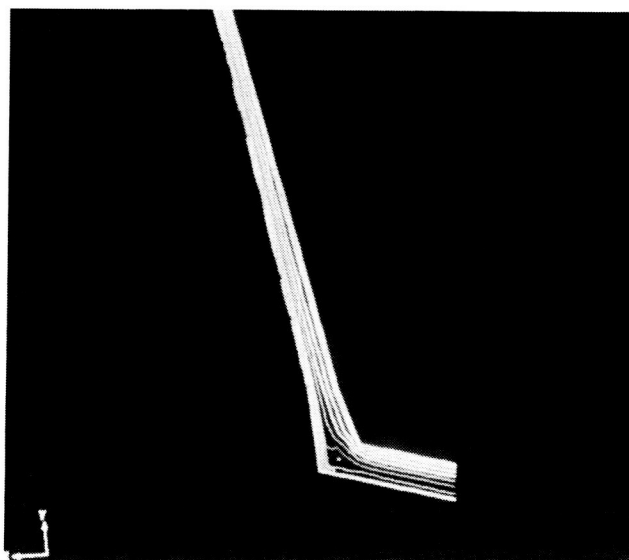
Effect of Viscosity on the
Momentum Boundary Layer
(Figure 20)

ORIGINAL PAGE
BLACK AND WHITE PHOTOGRAPH

ORIGINAL PAGE
BLACK AND WHITE PHOTOGRAPH

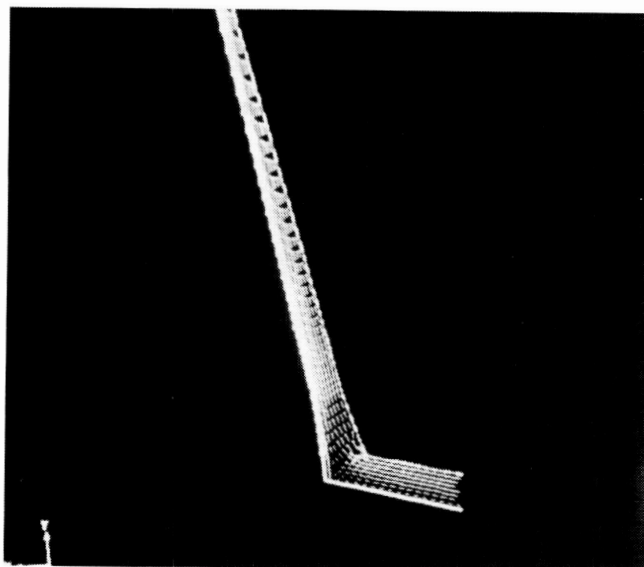


low
velocity

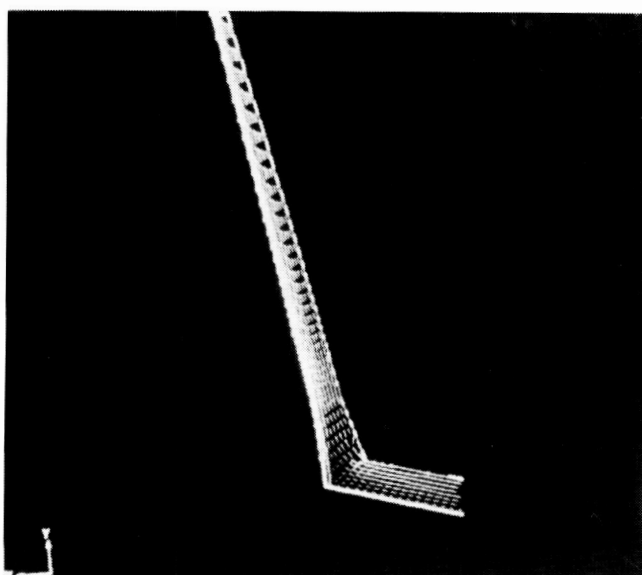


high
velocity

Effect of Velocity on the Size
of the Recirculation Zone
(Figure 21)



low
velocity

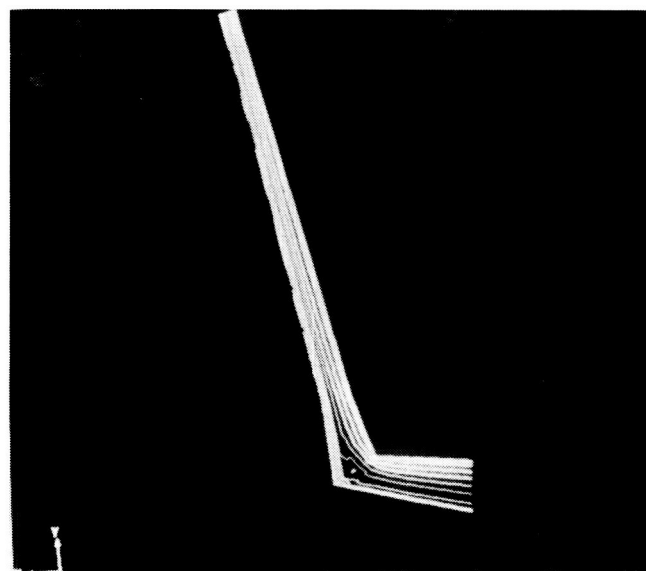
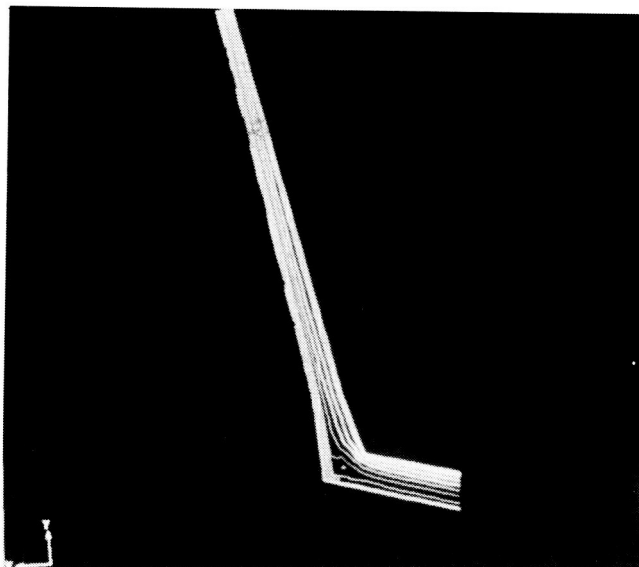


high
velocity

Effect of Velocity on the
Momentum Boundary Layer
(Figure 22)

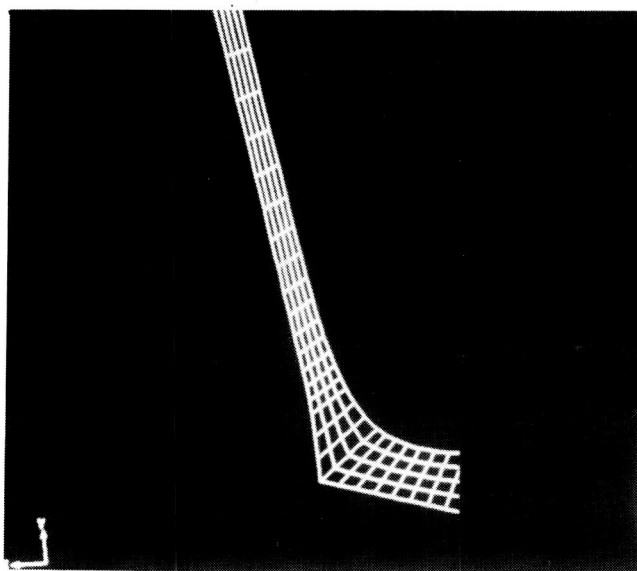
ORIGINAL PAGE
BLACK AND WHITE PHOTOGRAPH

ORIGINAL PAGE
BLACK AND WHITE PHOTOGRAPH

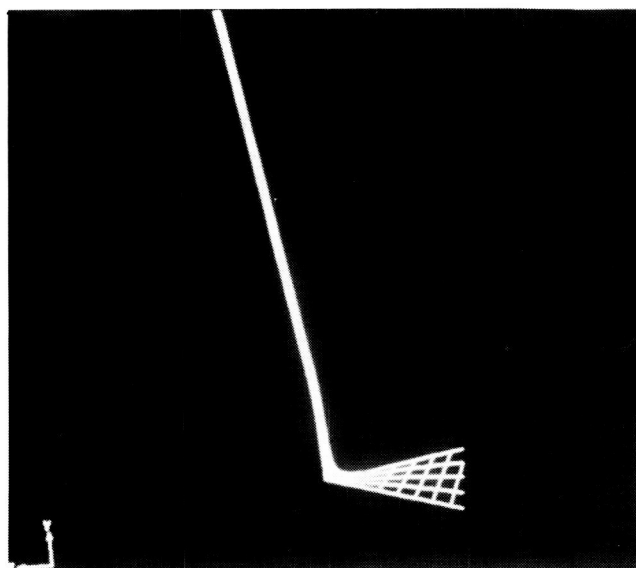


increased
melt
depth

Effect of Melt Depth on the Size
of the Recirculation Zone
(Figure 23)



low
viscosity

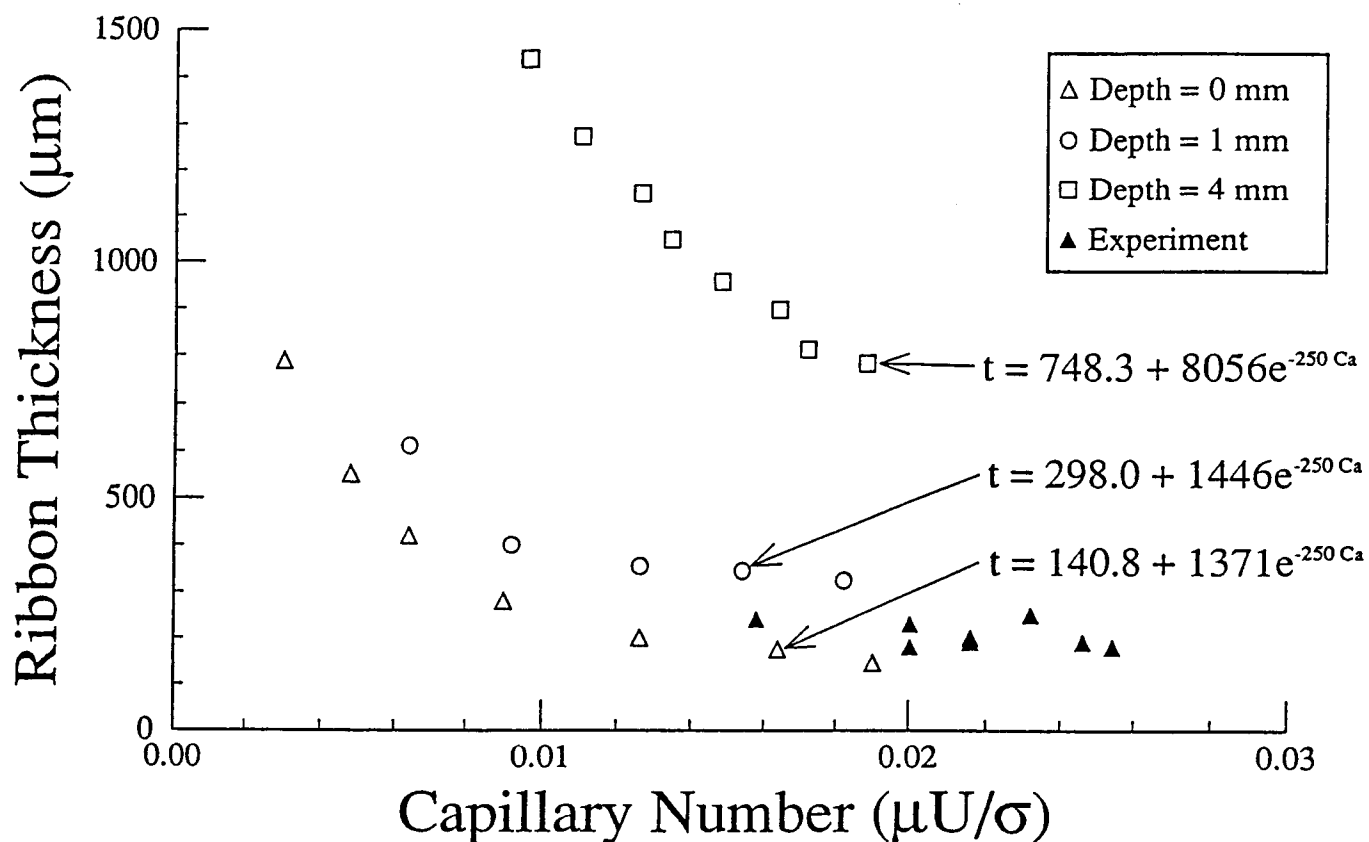


high
viscosity

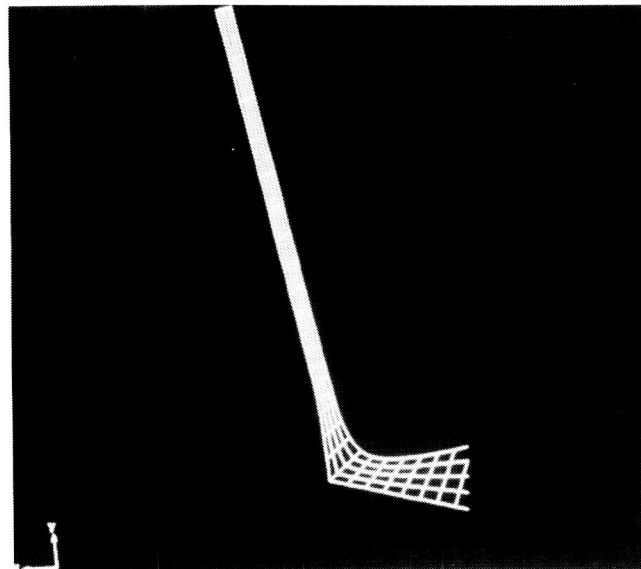
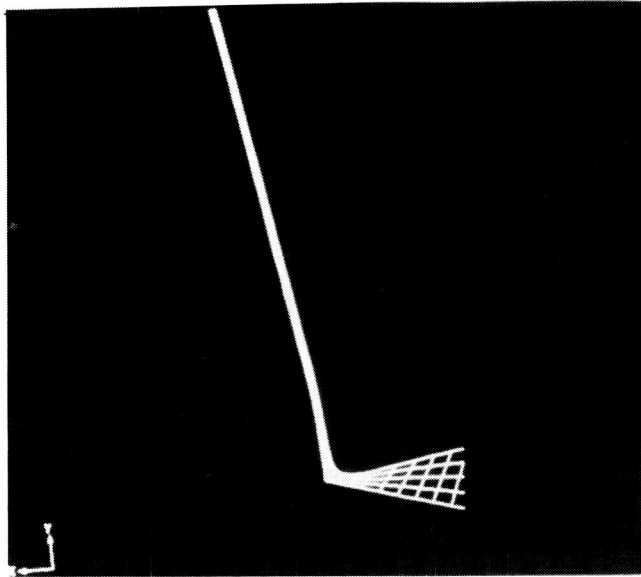
Effect of Viscosity on
Ribbon Thickness
(Figure 24)

ORIGINAL PAGE
BLACK AND WHITE PHOTOGRAPH

Computed vs. Measured Thickness



Effect of Capillary Number on
Ribbon Thickness
(Figure 25)

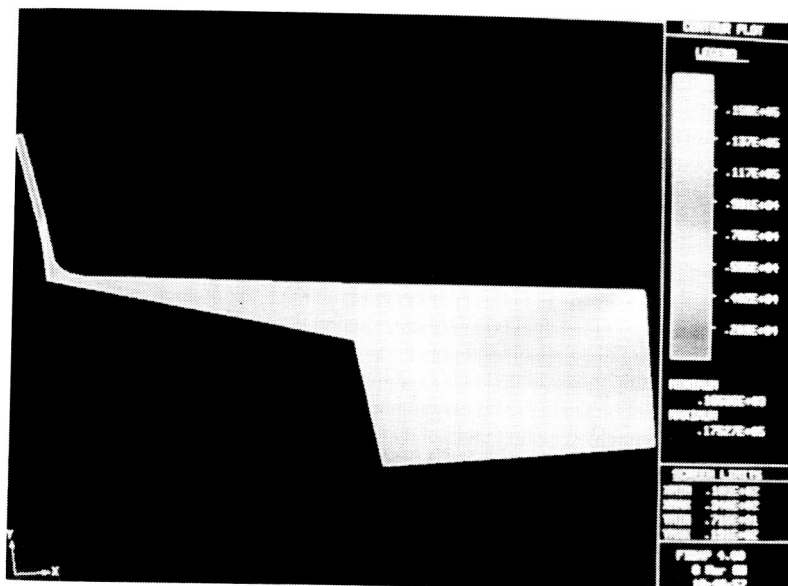
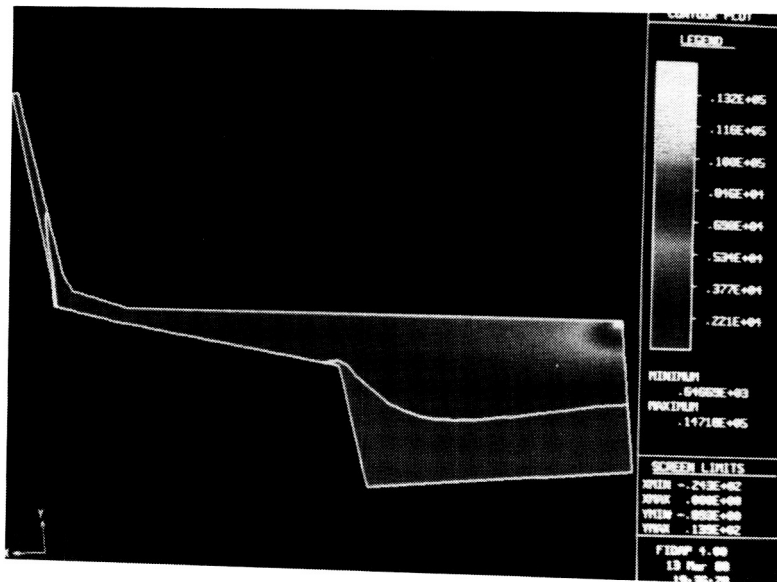


increased
melt
depth

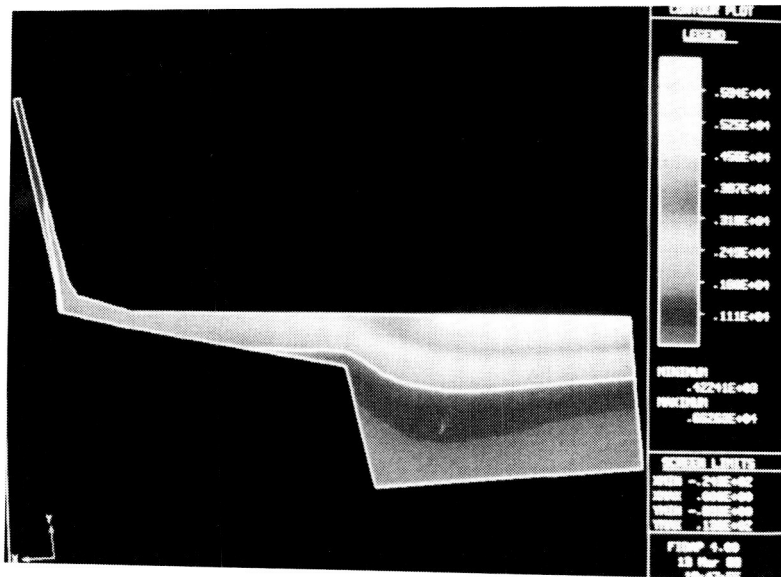
Effect of Melt Depth on
Ribbon Thickness
(Figure 26)

ORIGINAL PAGE
BLACK AND WHITE PHOTOGRAPH

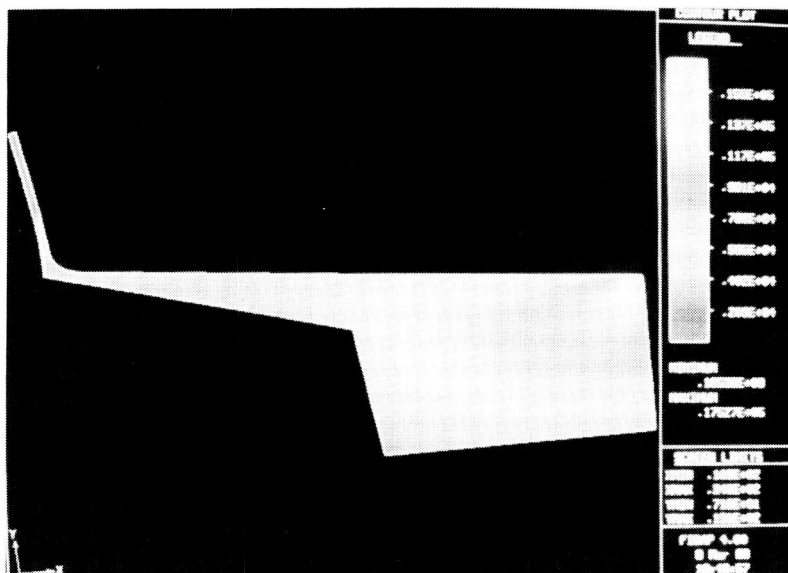
ORIGINAL PAGE
BLACK AND WHITE PHOTOGRAPH



Effect of Torch Intensity on
Temperature Profiles
(Figure 27)



Ramped



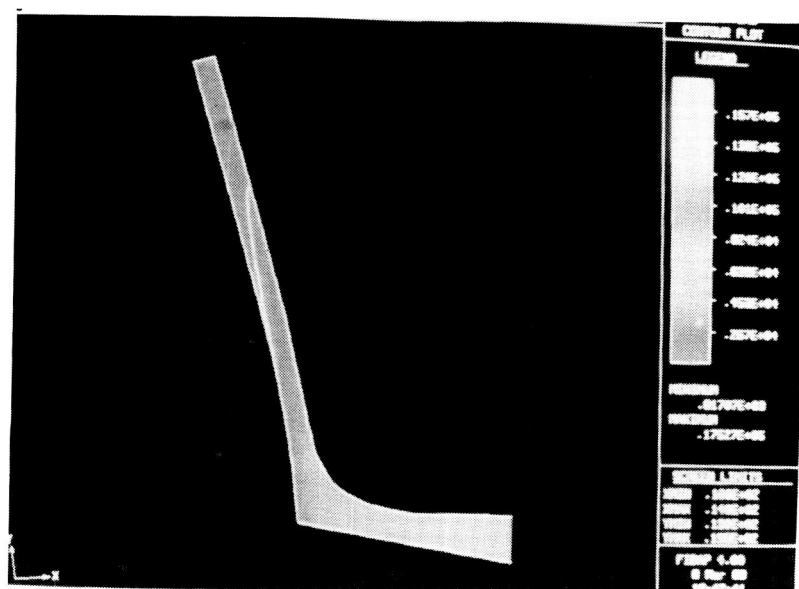
Gaussian

Effect of Ramped vs. Gaussian Torch Profile
on Temperature Profiles
(Figure 28)

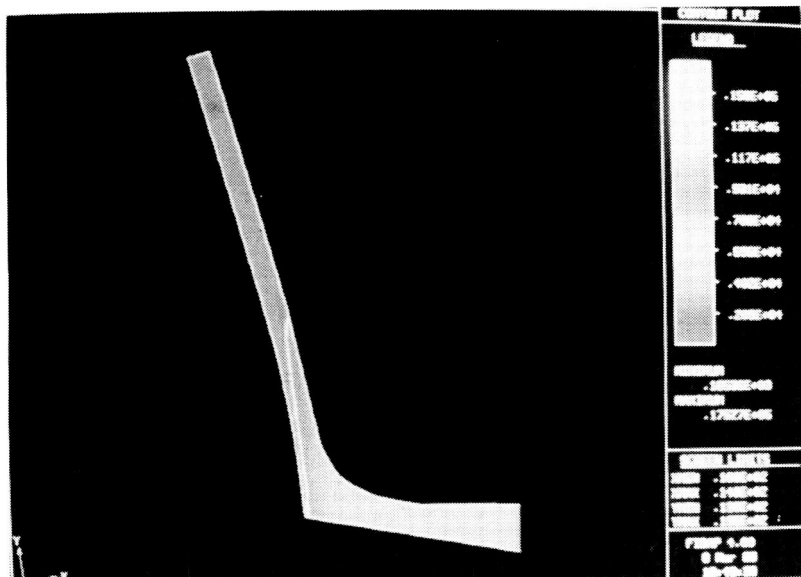
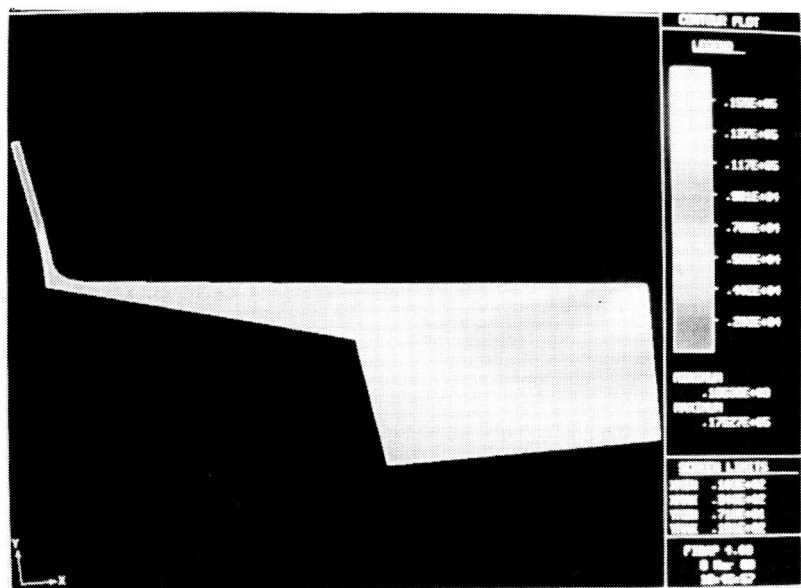
ORIGINAL PAGE
BLACK AND WHITE PHOTOGRAPH

CONTOUR PLOT

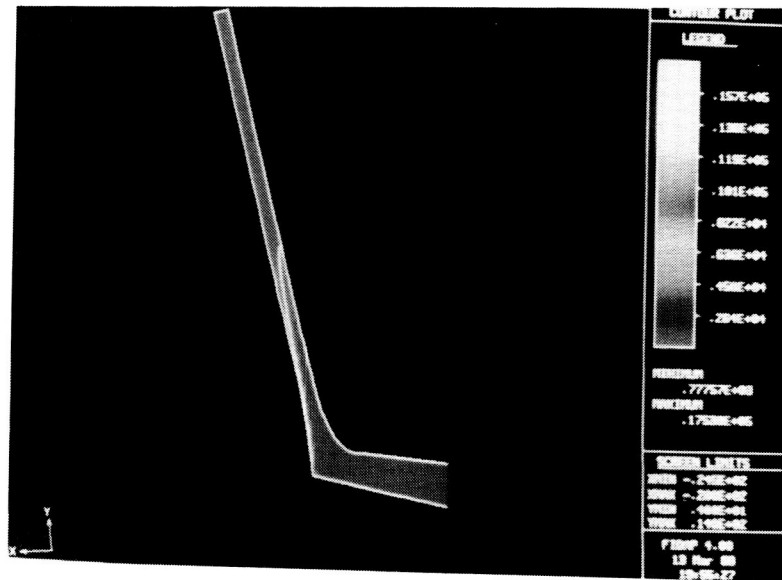
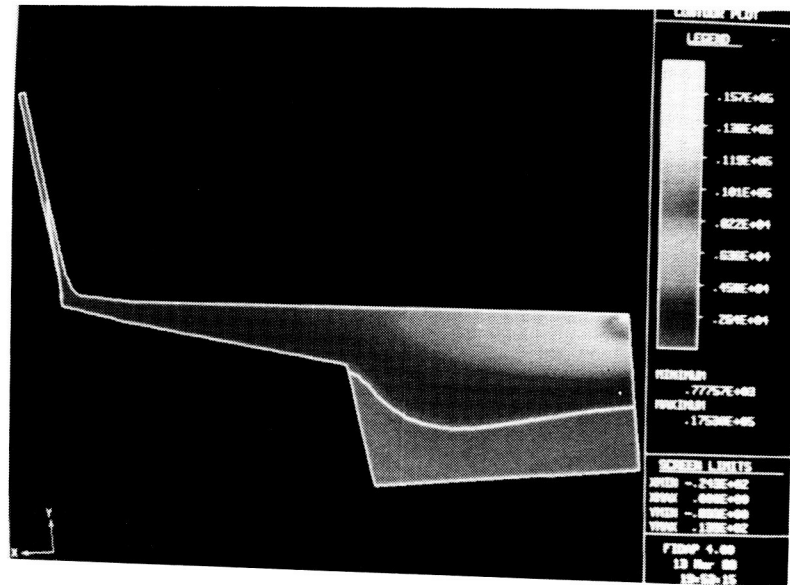
1.527E+06
1.188E+06
1.128E+06
1.068E+06
1.008E+06
948E+05
888E+05
828E+05
768E+05
708E+05
648E+05
588E+05
528E+05
468E+05
408E+05
348E+05
288E+05
228E+05
168E+05
108E+05
48E+05
-12E+05
-72E+05
-122E+05
-172E+05
-222E+05
-272E+05
-322E+05
-372E+05
-422E+05
-472E+05
-522E+05
-572E+05
-622E+05
-672E+05
-722E+05
-772E+05
-822E+05
-872E+05
-922E+05
-972E+05
-1022E+05
-1072E+05
-1122E+05
-1172E+05
-1222E+05
-1272E+05
-1322E+05
-1372E+05
-1422E+05
-1472E+05
-1522E+05
-1572E+05
-1622E+05
-1672E+05
-1722E+05
-1772E+05
-1822E+05
-1872E+05
-1922E+05
-1972E+05
-2022E+05
-2072E+05
-2122E+05
-2172E+05
-2222E+05
-2272E+05
-2322E+05
-2372E+05
-2422E+05
-2472E+05
-2522E+05
-2572E+05
-2622E+05
-2672E+05
-2722E+05
-2772E+05
-2822E+05
-2872E+05
-2922E+05
-2972E+05
-3022E+05
-3072E+05
-3122E+05
-3172E+05
-3222E+05
-3272E+05
-3322E+05
-3372E+05
-3422E+05
-3472E+05
-3522E+05
-3572E+05
-3622E+05
-3672E+05
-3722E+05
-3772E+05
-3822E+05
-3872E+05
-3922E+05
-3972E+05
-4022E+05
-4072E+05
-4122E+05
-4172E+05
-4222E+05
-4272E+05
-4322E+05
-4372E+05
-4422E+05
-4472E+05
-4522E+05
-4572E+05
-4622E+05
-4672E+05
-4722E+05
-4772E+05
-4822E+05
-4872E+05
-4922E+05
-4972E+05
-5022E+05
-5072E+05
-5122E+05
-5172E+05
-5222E+05
-5272E+05
-5322E+05
-5372E+05
-5422E+05
-5472E+05
-5522E+05
-5572E+05
-5622E+05
-5672E+05
-5722E+05
-5772E+05
-5822E+05
-5872E+05
-5922E+05
-5972E+05
-6022E+05
-6072E+05
-6122E+05
-6172E+05
-6222E+05
-6272E+05
-6322E+05
-6372E+05
-6422E+05
-6472E+05
-6522E+05
-6572E+05
-6622E+05
-6672E+05
-6722E+05
-6772E+05
-6822E+05
-6872E+05
-6922E+05
-6972E+05
-7022E+05
-7072E+05
-7122E+05
-7172E+05
-7222E+05
-7272E+05
-7322E+05
-7372E+05
-7422E+05
-7472E+05
-7522E+05
-7572E+05
-7622E+05
-7672E+05
-7722E+05
-7772E+05
-7822E+05
-7872E+05
-7922E+05
-7972E+05
-8022E+05
-8072E+05
-8122E+05
-8172E+05
-8222E+05
-8272E+05
-8322E+05
-8372E+05
-8422E+05
-8472E+05
-8522E+05
-8572E+05
-8622E+05
-8672E+05
-8722E+05
-8772E+05
-8822E+05
-8872E+05
-8922E+05
-8972E+05
-9022E+05
-9072E+05
-9122E+05
-9172E+05
-9222E+05
-9272E+05
-9322E+05
-9372E+05
-9422E+05
-9472E+05
-9522E+05
-9572E+05
-9622E+05
-9672E+05
-9722E+05
-9772E+05
-9822E+05
-9872E+05
-9922E+05
-9972E+05
-10022E+05
-10072E+05
-10122E+05
-10172E+05
-10222E+05
-10272E+05
-10322E+05
-10372E+05
-10422E+05
-10472E+05
-10522E+05
-10572E+05
-10622E+05
-10672E+05
-10722E+05
-10772E+05
-10822E+05
-10872E+05
-10922E+05
-10972E+05
-11022E+05
-11072E+05
-11122E+05
-11172E+05
-11222E+05
-11272E+05
-11322E+05
-11372E+05
-11422E+05
-11472E+05
-11522E+05
-11572E+05
-11622E+05
-11672E+05
-11722E+05
-11772E+05
-11822E+05
-11872E+05
-11922E+05
-11972E+05
-12022E+05
-12072E+05
-12122E+05
-12172E+05
-12222E+05
-12272E+05
-12322E+05
-12372E+05
-12422E+05
-12472E+05
-12522E+05
-12572E+05
-12622E+05
-12672E+05
-12722E+05
-12772E+05
-12822E+05
-12872E+05
-12922E+05
-12972E+05
-13022E+05
-13072E+05
-13122E+05
-13172E+05
-13222E+05
-13272E+05
-13322E+05
-13372E+05
-13422E+05
-13472E+05
-13522E+05
-13572E+05
-13622E+05
-13672E+05
-13722E+05
-13772E+05
-13822E+05
-13872E+05
-13922E+05
-13972E+05
-14022E+05
-14072E+05
-14122E+05
-14172E+05
-14222E+05
-14272E+05
-14322E+05
-14372E+05
-14422E+05
-14472E+05
-14522E+05
-14572E+05
-14622E+05
-14672E+05
-14722E+05
-14772E+05
-14822E+05
-14872E+05
-14922E+05
-14972E+05
-15022E+05
-15072E+05
-15122E+05
-15172E+05
-15222E+05
-15272E+05
-15322E+05
-15372E+05
-15422E+05
-15472E+05
-15522E+05
-15572E+05
-15622E+05
-15672E+05
-15722E+05
-15772E+05
-15822E+05
-15872E+05
-15922E+05
-15972E+05
-16022E+05
-16072E+05
-16122E+05
-16172E+05
-16222E+05
-16272E+05
-1632



A-53



Temperature Profiles for
wheel of 7.0
(Figure 30)



Temperature Profile for
Fully Coupled Problem
(Figure 31)

VII. Appendix I

Material Properties of Titanium

density	4.51	g/cm ³
surface tension	1600.	dyne/cm
surface tension angles	80.86	degrees
	185.0	"
thermal conductivity	0.41	cal/cm-s-C
emissivity	0.2	

Temperature Dependent Properties

viscosity.	0.01	g/cm-s	(< 1660 C)
	1x10 ²²	g/cm-s	(> 1670 C)
specific heat.	0.1	cal/g-C	(-1.0e12 to 1660 C)
	10.1	"	(1661 to 1670 C)
	0.1	"	(1671 to 1.0e12 C)
enthalpy	0.0		(0 C)
	270.0		(1660 C)
	365.0		(1671 C)
	615.0		(3500 C)
	1429.0		(10000 C)
heat transfer			
coefficient (wheel)	7.0	cal/cm ² -s-C	
heat transfer			
coefficient (crucible)	0.1	cal/cm ² -s-C	

reference

temperature 25.0 C

Stefan-Boltzman

constant $5.67\text{e-}12$

VIII. Appendix II

Velocity Solution Input File

*TITLE

MELT OVERFLOW PROCESS - VELOCITY SOLUTION

*FIMESH(IMAX=6,JMAX=3)

EXPI

/1 2 3 4 5 6

1 31 51 67 73 103

EXPJ

/1 2 3 4

1 7 15

POINT

1 1 1 1 0. 0.

2 2 1 1 10.244 0.

3 1 2 1 0. 3.75031

4 2 2 1 10.99083 4.71186

5 3 2 1 19.38125 6.86281

6 4 2 1 21.844 7.620

11 5 2 1 21.89888 8.79939

12 6 2 1 23.02756 15.95693

13 1 3 1 0. 5.64864

14 2 3 1 10.99083 6.52353

15 3 3 1 19.0 7.31093

/13 1 3 1 0. 5.83771

/14 2 3 1 10.99083 6.79929

/15 3 3 1 19.0 7.5

/16 4 3 1 21.1 8.2

16 4 3 1 21.1 8.3

/17 5 3 1 21.41962 8.87658

17 5 3 1 21.41962 9.1

18 6 3 1 22.78024 15.99342

19 0 0 0 34.544 7.620

LINE

1 2

```

1    3
2    4
3    4
4    5
5    6
13   14
14   15
15   16
16   17
17   18   4.   3
12   18
3    13
4    14
5    15
6    16
11   17

```

ARC

```
6    11    19
```

CURVE

```

11  12  5   4.   3
21.91199  8.93231
21.94259  9.19933
21.97917  9.46795
22.02190  9.73822
22.06840  9.99687

```

SURFACE

```

1    4
3    18

```

ELEMENT(QUAD,NODES=4,ALL)

ELEMENT(BOUNDARY,NODES=2)

```

12   18
1    2
1    2
2    4
2    4
4    6

```

```

4      6
ELEMENT(BOUNDARY,NODES=2,CRNS,CRNF)
6      12
6      12
ELEMENT(BOUNDARY,NODES=2,CRNS,CRNF)
18     13
18     13
BCNODE(UX)
12     18
6      12    20.
4      6
1      2
2      4
BCNODE(UX,FREE)
18     18
BCNODE(UY)
4      6
6      12
1      2
2      4
15     13
/tangential comp. of vel. set to zero for initial slip problem
/18     15
BCNODE(UX)
6      6    20.
BCNODE(UY)
13     13
BCNODE(UY,FREE)
15     15
BCNODE(SURFACE)
15     13    1.
NUMBER
2      1
SPINES
13     3     18
END

```

```

*PROBLEM(STEADY,NONLINEAR,FREE)
/*PROBLEM(STEADY,NONLINEAR)
/
*PRESSURE(MIXED DISCONTINUOUS)
*EXECUTION(NEWJOB)
*SOLUTION(N.R.=15,VELCONV=.001,RESCONV=.001)
*OPTIONS(STRESSDIVERGENCE)
*ICNODE(VELOCITY,READ)
*DATAPRINT(NONE)
*DENSITY(CONSTANT=4.51)
*VISCOSITY(CONSTANT=0.04)
*SURFACETENSION(CONSTANT=1600,ANG1=80.85,ANG2=185.0)
*NODES(FIMESH)
*ELEMENTS(QUAD,NODES=4,FIMESH)
*ELEMENTS(SLIP,NODES=2,FIMESH)
*ELEMENTS(SLIP,NODES=2,FIMESH)
*ELEMENTS(SLIP,NODES=2,FIMESH)
*ELEMENTS(SLIP,NODES=2,FIMESH)
*ELEMENTS(SLIP,NODES=2,FIMESH)
*ELEMENTS(SLIP,NODES=2,FIMESH)
*ELEMENTS(SLIP,NODES=2,FIMESH)
*ELEMENTS(SLIP,NODES=2,FIMESH)
*ELEMENTS(SLIP,NODES=2,FIMESH)
/*ELEMENTS(SLIP,NODES=2,FIMESH)
/*ELEMENTS(SLIP,NODES=2,FIMESH)
*ELEMENTS(SURFACE,NODES=2,FIMESH)
*ELEMENTS(SURFACE,NODES=2,FIMESH)
*PRINTOUT(NONE)
*END

```

IX. Appendix III

Temperature Solution Input File

```
*TITLE
MELT OVERFLOW RIBBON SIMULATION - TEMPERATURE
/*PROBLEM(STEADY, NONLINEAR, 2-D, ADV-DIF)
/*PROBLEM(STEADY, NONLINEAR, 2-D, ADV-DIF, FREE)
*PROBLEM(STEADY, NONLINEAR, 2-D, STRONGLY-CPLD)
/*PROBLEM(STEADY, NONLINEAR, 2-D, STRONGLY-CPLD, FREE)
*PRESSURE(MIXED DISCONTINUOUS)
*EXECUTION(NEWJOB)
/*EXECUTION(RESTART)
*SOLUTION(Q.N.=10, VELC=.001, RESCONV=.001, ACCF=.5)
*ICNODE(VELOCITY, READ)
/*ICNODE(TEMPERATURE, READ)
*DATAPRINT(NONE)
/ TITANIUM PROPERTY DATA
*DENSITY(SET=1, CONSTANT=4.51)
*VISCOSITY(SET=1, CURVE=4)
-1.0E12, 1660, 1671, 1.0E12, 1.0E22, 1.0E22, .01, .01
/*SPECIFICHEAT(SET=1, CURVE=6)
/-3.0E12, 1660, 1661, 1670, 1671, 3.0E12
/0.1, 0.1, 10.1, 10.1, 0.1, 0.1
*SPECIFICHEAT(SET=1, SUBROUTINE=12)
5, 1
0.0, 1660, 1671, 3500, 10000
0.0, 270, 365, 615, 1429
*CONDUCTIVITY(SET=1, CONSTANT=0.41)
*SURFACETENSION(SET=1, CONSTANT=1600, ANG1=80.85, ANG2=5)
*VOLUMEXPANSION(SET=1, CONSTANT=0., REFTEMP=25)
*NODES(CARTESIAN, FIMESH)
*HTRANSFER(SET=1, CONSTANT=7.0, REFTEMP=25)
*HTRANSFER(SET=2, CONSTANT=0.1, REFTEMP=25)
*EMISSIVITY(SET=1, CONSTANT=0.2, REFTEMP=25, STEFB=5.67E-12)
```

```

*ELEMENTS(QUAD,NODES=4,FIMESH,ALL,MDENS=1,MVISC=1,MSPHT=1,MCOND=1,M
EXP=1)
*ELEMENTS(SLIP,NODES=2,FIMESH)
*ELEMENTS(CONVECTION,NODES=2,FIMESH,MCNV=2)
*ELEMENTS(SLIP,NODES=2,FIMESH)
*ELEMENTS(CONVECTION,NODES=2,FIMESH,MCNV=2)
*ELEMENTS(SLIP,NODES=2,FIMESH)
*ELEMENTS(CONVECTION,NODES=2,FIMESH,MCNV=1)
*ELEMENTS(SLIP,NODES=2,FIMESH)
*ELEMENTS(CONVECTION,NODES=2,FIMESH,MCNV=1)
/*ELEMENTS(SLIP,NODES=2,FIMESH)
*ELEMENTS(SURFACE,NODES=2,FIMESH)
*BCNODE(HEAT,NODES=2)
1773,1774,1,0,9.65625
1804,1805,0,299.34375,309
1805,1806,0,309,1927
1806,1807,0,1927,12332
1807,1808,0,12332,77076
*END

```

X. References

1. L. E. Hackman and T. Gasper: Industrial Heating, Jan 1986, p. 23.
2. S. Kavesch: in Metallic Glasses, J. Gilman and H. Leamy, eds., American Society for Metals, Metals Park, OH, pp36-40.
3. T. Anthony and H. Cline: Journal of Applied Physics, 1978, vol 49, pp 829-832.
4. W. Kurz and D.J. Fisher: Fundamentals of Solidification, Trans Tech Publications, Aedermannsdorf, Switzerland, 1986, p. 91.
5. M.S. Engelman: FIDAP Theoretical Manual, Fluid Dynamics International, Evanston,IL, 1987, p. 1-1.
6. M.S. Engelman: FIDAP Theoretical Manual, Fluid Dynamics International, Evanston,IL, 1987, p. 10-1.
7. A.D. Agayev, V.I. Kostikov, and V.N. Bobkovskiy: Russian Metallurgy, 1980, Vol. 3, pp.33-35.
8. E. Lemmon: Numerical Methods in Heat Transfer, John Wiley and Sons, New York, 1981.
9. J.A. Dantzig: Personal Conversation
10. M.S. Engelman: FIDAP Theoretical Manual, Fluid Dynamics International, Evanston,IL, 1987, p. 10-9.
11. M.S. Engelman: FIDAP Theoretical Manual, Fluid Dynamics International, Evanston,IL, 1987, p. 8-1
12. M.S. Engelman: FIPREP Users Manual, Fluid Dynamics International, Evanston,IL, 1987, pp. 10-7 - 10-17.

13. E.M. Gutierrez and J. Szekely: Metallurgical Transactions, Dec. 1986, Vol. 17B, pp. 695-703.
14. J.A. Dantzig and J.W. Kelly: unpublished research, University of Illinois at Urbana-Champaign, 1988.
15. H.W. Deem and C.F. Lucks: Survey of Physical Property Data for Titanium and Titanium Alloys, Battelle Memorial Institute, Columbus, OH, 1956, p. 19.
16. M.S. Engelman: FIDAP Theoretical Manual, Fluid Dynamics International, Evanston, IL, 1987, p. 2-6.
17. M.S. Engelman: FIDAP Theoretical Manual, Fluid Dynamics International, Evanston, IL, 1987, p. 10-7.



Report Documentation Page

1. Report No. NASA CR-4253	2. Government Accession No.	3. Recipient's Catalog No.	
4. Title and Subtitle Rapidly Solidified Titanium Alloys by Melt Overflow		5. Report Date September 1989	
		6. Performing Organization Code	
7. Author(s) Thomas A. Gaspar, Thomas J. Bruce, Jr., Lloyd E. Hackman, Susan E. Brasmer, Jonathan A. Dantzig, and William A. Baeslack III		8. Performing Organization Report No.	
		10. Work Unit No. 324-02-00	
9. Performing Organization Name and Address Ribbon Technology Corporation Box 30758 Gahanna, OH 43230		11. Contract or Grant No. NAS1-18288	
		13. Type of Report and Period Covered Contractor Report	
12. Sponsoring Agency Name and Address National Aeronautics and Space Administration Langley Research Center Hampton, VA 23665-5225		14. Sponsoring Agency Code	
15. Supplementary Notes Langley Technical Monitor: R. Keith Bird (SBIR Phase II. Final Report) T.A. Gaspar , T.J. Bruce and L.E. Hackman: Ribbon Technology Corp., Gahanna, OH. S.E. Brasmer and J.A. Dantzig: University of Illinois, Urbana, Illinois. W.A. Baeslack III: The Ohio State University, Columbus, OH. Appendix A of this report was offered as a thesis in partial fulfillment of the requirements of a Master of Science in Mechanical Engineering, University of Illinois, Urbana, IL.			
16. Abstract A pilot plant scale furnace was designed and constructed for casting titanium alloy strip. The furnace combines plasma arc skull melting techniques with melt overflow rapid solidification technology. A mathematical model of the melting and casting process was developed. The furnace cast strip of a suitable length and width for use with honeycomb structures. Titanium alloys Ti-6Al-4V and Ti-14Al-21Nb were successfully cast into strip. The strip was evaluated by optical metallography, microhardness, chemical analysis and cold rolling.			
17. Key Words (Suggested by Author(s)) Rapid Solidification Titanium Alloys		18. Distribution Statement Unclassified-Unlimited Subject Category 26	
19. Security Classif. (of this report) Unclassified	20. Security Classif. (of this page) Unclassified	21. No. of pages 100	22. Price A05